

# The MUSE-Wide Survey: A determination of the Lyman $\alpha$ emitter luminosity function at $3 < z < 6$

Edmund Christian Herenz<sup>1</sup>, Lutz Wisotzki<sup>2</sup>, Rikke Saust<sup>2</sup>, Josephine Kerutt<sup>2</sup>, Tanya Urrutia<sup>2</sup>, Catrina Diener<sup>3</sup>, Kasper Borello Schmidt<sup>2</sup>, Raffaella Anna Marino<sup>4</sup>, Geoffroy de la Vieuville<sup>5</sup>, Leindert Boogaard<sup>6</sup>, Joop Schaye<sup>6</sup>, Bruno Guiderdoni<sup>7</sup>, Johan Richard<sup>7</sup>, and Roland Bacon<sup>7</sup>

<sup>1</sup> Department of Astronomy, Stockholm University, AlbaNova University Centre, SE-106 91, Stockholm, Sweden

<sup>2</sup> Leibniz-Institut für Astrophysik Potsdam (AIP), An der Sternware 16, 14482 Potsdam, Germany

<sup>3</sup> University of Cambridge, Madingley Road, Cambridge CB3 0HA, UK

<sup>4</sup> ETH Zürich, Department of Physics, Wolfgang-Pauli-Strasse 27, 8093 Zürich, Switzerland

<sup>5</sup> Institut de Recherche en Astrophysique et Planétologie (IRAP), Université de Toulouse, CNRS, UP, CNES, 14 avenue Edouard Belin, F-31400 Toulouse, France

<sup>6</sup> Leiden Observatory, Leiden University, PO Box 9513, 2300 RA Leiden, The Netherlands

<sup>7</sup> Univ Lyon, Univ Lyon1, Ens de Lyon, CNRS, Centre de Recherche Astrophysique de Lyon UMR5574, F-69230, Saint-Genis-Laval, France

November 30, 2019

## ABSTRACT

We investigate the Lyman  $\alpha$  emitter luminosity function (LAE LF) within the redshift range  $2.9 \leq z \leq 6$  from the first instalment of the blind integral field spectroscopic survey MUSE-Wide. This initial part of the survey probes a region of  $22.2 \text{ arcmin}^2$  in the CANDELS/GOODS-S field (24 MUSE pointings with 1h integrations). The dataset provided us with 237 LAEs from which we construct the LAE LF in the luminosity range  $42.2 \leq \log L_{\text{Ly}\alpha} [\text{erg s}^{-1}] \leq 43.5$  within a volume of  $2.3 \times 10^5 \text{ Mpc}^3$ . For the LF construction we utilise three different non-parametric estimators: The classical  $1/V_{\text{max}}$  method, the  $C^-$  method, and an improved binned estimator for the differential LF. All three methods deliver consistent results, with the cumulative LAE LF being  $\Phi(\log L_{\text{Ly}\alpha} [\text{erg s}^{-1}] = 43.5) \approx 3 \times 10^{-6} \text{ Mpc}^{-3}$  and  $\Phi(\log L_{\text{Ly}\alpha} [\text{erg s}^{-1}] = 42.2) \approx 2 \times 10^{-3} \text{ Mpc}^{-3}$  towards the bright- and faint-end of our survey, respectively. By employing a non-parametric statistical test, as well as by comparing the full sample to sub-samples in redshift bins, we find no supporting evidence for an evolving LAE LF over the probed redshift and luminosity range. Using a parametric maximum-likelihood technique we determine the best-fitting Schechter function parameters  $\alpha = -1.84^{+0.42}_{-0.41}$  and  $\log L^* [\text{erg s}^{-1}] = 42.2^{+0.22}_{-0.16}$  with the corresponding normalisation  $\log \phi^* [\text{Mpc}^{-3}] = -2.71$ . However, the dynamic range in  $\text{Ly}\alpha$  luminosities probed by MUSE-Wide leads to a strong degeneracy between  $\alpha$  and  $L^*$ . Moreover, we find that a power-law parameterisation of the LF appears to be less consistent with the data compared to the Schechter function, even so when not excluding the X-Ray identified AGN from the sample. When correcting for completeness in the LAE LF determinations, we take into account that LAEs exhibit diffuse extended low surface-brightness haloes. We compare the resulting LF to one obtained where we apply a correction assuming compact point-like emission. We find that the standard correction underestimates the LAE LF at the faint end of our survey by a factor of 2.5. Contrasting our results to the literature we find that at  $\log L_{\text{Ly}\alpha} [\text{erg s}^{-1}] \lesssim 42.5$  previous LAE LF determinations from narrow-band surveys appear to be affected by a similar bias.

**Key words.** Cosmology: observations – Galaxies: high-redshift – Galaxies: luminosity function – Techniques: imaging spectroscopy

## 1. Introduction

One of the most fundamental statistical distribution functions to characterise the population of galaxies is the galaxy luminosity function (LF). The differential LF,  $\psi(L, z)$ , counts the number of galaxies  $N$  per unit volume  $V$  as a function of luminosity  $L$  and redshift  $z$ :  $dN = \psi(L, z) dL dV dz$ . While this bi-modal form provides the most general description, observationally the LF is often determined at a fixed redshift or a redshift interval over which effects of redshift evolution are deemed negligible, i.e

$$dN = \phi(L) dL dV . \quad (1)$$

Galaxy LFs and their redshift evolution provide a gold standard for summarising the changing demographics of galaxies with cosmic look-back time. Being essential benchmarks for cosmological models of galaxy formation and evolution in our universe, LF determinations are often amongst the pivotal goals in

the design and analysis of extragalactic surveys (Petrosian 1992; Willmer 1997; Johnston 2011; Dunlop 2013; Caditz 2016).

While Lyman  $\alpha$  ( $\text{Ly}\alpha$ ,  $\lambda 1216$ ) emission was already suggested as a prime tracer for galaxy formation studies in the early universe more than five decades ago (Partridge & Peebles 1967), initial searches for such high- $z$   $\text{Ly}\alpha$  emitting galaxies (LAEs) were unsuccessful and, hence, constrained only upper limits of the LAE LF (see review by Pritchett 1994).

The first successful detections of LAEs accompanied by spectroscopic confirmations on 8 m class telescopes employed a colour-excess criterion in narrow-band (NB) images (Hu & McMahon 1996; Hu et al. 1998). In the following years the NB imaging technique was routinely used to construct LAE samples of up to several hundreds of galaxies at  $2 \lesssim z \lesssim 5$  (see review by Taniguchi et al. 2003). Mostly from such NB surveys, sometimes in combination with spectroscopic follow-up of sub-samples, the

first LAE LF estimates up to  $z \sim 6$  were obtained (e.g., Cowie & Hu 1998; Kudritzki et al. 2000; Ouchi et al. 2003; Hu et al. 2004; Ajiki et al. 2004; Tapken et al. 2006; Dawson et al. 2007; Gronwall et al. 2007; Murayama et al. 2007; Sawicki et al. 2008; Henry et al. 2012).

Most of the LAE LF studies so far focused on a single redshift slice of typically  $\Delta z \approx 0.1$  (corresponding to typical NB filter widths  $\Delta\lambda \approx 100\text{\AA}$ ). Significant progress in terms of methodology, numbers of LAEs, and rate of spectroscopic follow-up observations was achieved by Ouchi et al. (2008) within three redshift slices ( $z \sim \{3, 4, 5\}$ ) over a  $1\text{ deg}^2$  region in the *Subaru*/XMM-Newton Deep Survey (SXDS; Furusawa et al. 2008). Later, Ouchi et al. (2010) extended the SXDS LAE survey to  $z \approx 6.6$ . More recently, further *Subaru*/Suprime-Cam NB imaging data in other fields were used to construct LAE LFs over  $5\text{ deg}^2$  at  $z = 5.7$  and  $z = 6.6$  (Matthee et al. 2015; Santos et al. 2016). Moreover, by combining NB and medium-band observations from the Subaru and the Isaac Newton Telescope Sobral et al. (2018b) constructed a LAE LF from  $\sim 4000$  LAEs simultaneously from redshifts  $z \sim 2$  to  $z \sim 6$ .

The latest development in NB LAE surveys is due to the advent of *Subaru*/Hyper Suprime-Cam, a  $1.5\text{ deg}^2$  wide-field imager (Miyazaki et al. 2012, 2018). Recently, the first results for a  $\sim 14\text{ deg}^2$  and  $\sim 21\text{ deg}^2$  NB survey at  $z \sim 6$  and  $z \sim 7$ , respectively, were published (the so called SILVERUSH survey Ouchi et al. 2018; Shibuya et al. 2018b,a). From this unprecedented dataset Konno et al. (2018) constructed the LAE LF for sources  $L_{\text{Ly}\alpha} \gtrsim 10^{43}\text{ erg s}^{-1}$ . Without any doubt NB imaging studies have been and are still of central importance for our understanding of the LAE LF. Only their wide nature allows the construction of statistical samples of the brightest and rarest LAEs.

However, the LAE LF determination from NB imaging studies is fraught with some difficulties that can be alleviated in blind surveys with an integral field spectrograph (IFS, see e.g. the recent textbook by Bacon & Monnet 2017). Especially, since an IFS samples spectra over a contiguous field of view, the resulting 3D datacubes can be envisioned as a stack of narrow-band images of much smaller bandwidth compared to imaging narrow-band filters. Thus, a blind search for emission line sources in an IFS datacube provides directly a catalogue of spectroscopically confirmed Ly $\alpha$  emitters, avoiding the need for follow-up spectroscopy. Then, flux measurements on the lines can be performed in virtually any conceivable aperture, resulting in reliable flux measurements absent of slit- or bandpass- losses. Moreover, instead of probing only a tiny redshift slice, IFSs cover an extended range in redshifts. Another advantage is that the narrow bandwidth of the individual wavelength slices in the datacube significantly reduces the contribution of sky background to emission line signals. This allows IFS searches to reach significant fainter limiting fluxes compared to NB imaging surveys. Lastly, by construction an integral field spectroscopic survey delivers a flux-limited LAE sample, rather than an equivalent-width limited sample. This mitigates possible biases from heterogeneous equivalent width cuts in NB imaging studies.

A pilot IFS survey for LAEs between  $3 < z < 6$  was performed by van Breukelen et al. (2005) with the Visible Multi Object Spectrograph (Le Fèvre et al. 2003) Integral Field Unit at ESOs Very Large Telescope (VLT). However, this pilot study was severely limited by the relatively low throughput, small field of view, and the low spectral resolution of this instrument. Substantial progress in performing a blind IFS survey to detect Ly $\alpha$  emitters was achieved in the Hobby Eberle Telescope Dark Energy Experiment (HETDEX) Pilot Survey by Adams et al. (2011). Utilising 61 nights of observations with VIRUS-P (Hill

et al. 2008), a path-finder fiber-fed IFS that will be replicated 156 times for the final HETDEX survey (Hill & HETDEX Consortium 2016), on the McDonald 2.7m Harlan J. Smith telescope, Adams et al. constructed a catalogue of 397 emission line galaxies blindly selected over  $169\text{ arcmin}^2$  in areas with rich complementary datasets. This catalogue contained 99 LAEs without X-ray counterparts between  $1.9 < z < 3.8$ . From the Adams et al. catalogue Blanc et al. (2011) constructed the Ly $\alpha$  LF in the luminosity range  $42.6 \leq \log L_{\text{Ly}\alpha} [\text{erg s}^{-1}] \leq 43.5$ .

With the advent of the Multi Unit Spectroscopic Explorer at ESOs VLT (MUSE, Bacon et al. 2014; Caillier et al. 2014) the field of blind deep IFS surveys was revolutionised. This image-slicer based IFS with a  $1' \times 1'$  field of view covering the wavelength range from  $4650\text{\AA}$  to  $9300\text{\AA}$  was designed from the ground up as a discovery machine for faint emission line galaxies, especially LAEs at high redshift ( $2.9 \lesssim z \lesssim 6.6$ , Bacon et al. 2004).

Its unprecedented potential for LAE LF determinations was demonstrated in the analysis of a 27h integration on the *Hubble* Deep Field South (Casertano et al. 2000) obtained during commissioning (Bacon et al. 2015). By utilising 59 LAEs from this dataset Drake et al. (2017b) could put constraints the Ly $\alpha$  LF down to  $\log L_{\text{Ly}\alpha} [\text{erg s}^{-1}] = 41.4$ , almost an order of magnitude deeper than **almost all previous** observational efforts, with the only exception being a heroic 92h deep long-slit integration with the FORS2 instrument on ESOs VLT (Rauch et al. 2008). Recently, the Drake et al. (2017b) pilot-study was significantly refined by Drake et al. (2017a) using 601 LAEs found in the MUSE Consortium Guaranteed Time Observations (GTO, Bacon et al. 2017; Inami et al. 2017) of the *Hubble* Ultra Deep Field (Beckwith et al. 2006). This dataset consists of a  $3.15' \times 3.15'$  mosaic exposed at 10h depth, and a central  $1.15\text{ arcmin}^2$  31h deep pointing that reached similar depths as the pilot study in the *Hubble* Deep field South. As a novelty Drake et al. (2017a) accounted for the effect of extended low-surface brightness Ly $\alpha$  haloes in their completeness assessment.

However, the pencil beam nature of the MUSE-deep fields does not allow to probe the LAE LF at brighter luminosities. Thus, complementary to the MUSE Deep Fields a shallower large-area programme, dubbed MUSE-Wide, is also part of the MUSE GTO. MUSE-Wide aims at covering  $100\text{ arcmin}^2$  at 1h depth in regions where deep HST imaging surveys were performed, namely the CANDELS/Deep region in the *Chandra* Deep Field South (Grogin et al. 2011; Koekemoer et al. 2011, CDFS) and the GOODS/South survey (Giavalisco et al. 2004). Recently, Herenz et al. (2017) (hereafter H017) presented a catalogue of 831 emission line selected galaxies from the first 24 MUSE-Wide pointings (corresponding to an area of  $22.2\text{ arcmin}^2$ ) in the CDFS. This catalogue contains 237 LAEs with luminosities  $41.6 \leq \log L_{\text{Ly}\alpha} [\text{erg s}^{-1}] \leq 43.5$  in the redshift range  $3 < z < 6$ , thus augmenting the sample of faint LAEs from the MUSE-Deep fields. In the present manuscript we will utilise the LAE sample obtained in the first 24 MUSE-Wide pointings for studying the LAE LF.

The structure of this manuscript is as follows: In Sect. 2 we provide an overview of the utilised MUSE-Wide survey data and we describe how we obtained the LAE initial sample from this dataset. Following, in Sect. 3 we explain how we construct the LAE selection function in MW. Then, in Sect. 4 we provide an overview of the adopted methods for constructing the LAE LF. Our results on the LAE LF are given in Sect. 5. In Sect. 6 we compare our results with the literature. Finally, we summarise the results obtained so far in Sect. 7, where we also present an

outlook for further refinements of our study that will be relevant with the release of the full MUSE-Wide sample.

Throughout the paper we always assume a standard  $\Lambda$ CDM concordance cosmology with  $\Omega_\Lambda = 0.7$ ,  $\Omega_M = 0.3$ , and  $H_0 = 70 \text{ km s}^{-1}$  when converting observed to physical quantities.

## 2. MUSE-Wide data and Ly $\alpha$ emitter sample

The data under scrutiny in this paper are the 24 adjacent  $1' \times 1'$  one hour deep MUSE pointings in the CANDELS/Deep region of the GOODS-South field. The data were taken during the first period of MUSE GTO Observations between September and October 2014 (ESO programme ID 094.A-0205) as part of the MUSE-Wide (MW hereafter) survey. Accounting for the  $4''$  overlap between individual pointings, the total survey area is  $22.2 \text{ arcmin}^2$ . The survey covers a wavelength range from  $4750 \text{ \AA}$  to  $9350 \text{ \AA}$ , thus probes Ly $\alpha$  emitters within the redshift range  $2.9 \leq z \leq 6.7$ .

A detailed account of the observations, data reduction, and construction of the emission line selected galaxy catalogue has been given in H017, here we only provide an overview.

### 2.1. Observations and Data Reduction

Each 1h deep MW pointing consists of four individual 15 minute exposures. More than half of the observations were taken under photometric conditions during dark and grey nights, with the remainder taken under clear conditions during dark nights. The measured seeing ranged from  $0.7''$  to  $1.1''$ , with  $0.9''$  being the average of the observations.

For each of the pointings a datacube was created by employing the MUSE data reduction system (Weilbacher et al. 2014) in combination with a few custom developed routines and the *Zurich Atmosphere Purge* (ZAP) sky-subtraction software<sup>1</sup> (Soto et al. 2016a). We also used the self-calibration procedure that is part of the MUSE Python Data Analysis Framework – MPDAF<sup>2</sup> (Conseil et al. 2016; Bacon et al. 2017).

The reduced data consists of 24 datacubes, each covering  $1' \times 1'$  on the sky with a spatial sampling  $0.2'' \times 0.2''$ . These spatial sampling elements (so-called spaxels) contain a spectrum from  $4750 \text{ \AA}$ – $9350 \text{ \AA}$  that is sampled at  $1.25 \text{ \AA}$  in air wavelengths. Each volume element (a so-called voxel) of a datacube stores the received flux density in units of  $10^{-20} \text{ erg s}^{-1} \text{ cm}^{-2} \text{ \AA}^{-1}$ . The full width at half maximum (FWHM) of the spectrographs line spread function is roughly twice the spectral sampling (i.e.  $\sim 2.5 \text{ \AA}$ ) resulting in a resolving power of  $R \sim 1900$ – $3800$  over the covered wavelength range.

The MUSE data reduction system also propagates the variances during all reduction steps into each voxel, thereby creating a complementary variance datacube for each pointing. However, these formal variance values underestimate the true variances, and are thus not optimal for emission line detection and estimation of the error on emission line flux measurements. In order to correct for this, we performed an empirical estimate of the variance values by evaluating the statistics of randomly placed apertures in empty regions of the sky (see Sect. 3.1.1 in H017).

<sup>1</sup> ZAP is publicly available via the Astrophysics Source Code Library: <http://ascl.net/1602.003> (Soto et al. 2016b).

<sup>2</sup> MPDAF is publicly available via the Astrophysics Source Code Library: <http://ascl.net/1611.003> (Piqueras et al. 2017).

### 2.2. Emission Line Galaxy Catalogue

Emission line source detection in the MW data is performed with our dedicated *Line Source Detection and Cataloguing Tool* LSDCat<sup>3</sup> (Herenz & Wisotzki 2017). As a required preparatory step before emission line source detection we remove source continua from the datacube by subtracting a  $\approx 190 \text{ \AA}$  wide running median in the spectral direction. This method of removing source continua has proven to be very effective, leaving as remaining features mostly real emission lines and straight-forward identifiable residuals from continua that vary at higher frequencies than the width of the median filter (e.g. cold stars).

In the next step LSDCat cross-correlates each datacube with a 3D matched filter template for compact emission line sources. We used a 3D Gaussian as the template, with its spatial FWHM dictated by the wavelength dependent seeing PSF and its spectral FWHM fixed to  $v_{\text{FWHM}} = 250 \text{ km s}^{-1}$ . As demonstrated in Sect. 4.3 of Herenz & Wisotzki (2017), the latter value is optimal for detecting LAEs in MUSE surveys at their highest possible signal-to-noise (S/N) ratios. Then the initial emission line candidate catalogue was created by setting the detection threshold to  $S/N_{\text{thresh}} = 8$ . This initial catalogue was then screened by four investigators (ECH, LW, TU, and JK) using the interactive graphical tool *QtClassify*<sup>4</sup> (Kerutt 2017; see also Appendix of H017). The purpose of this screening process was to identify the detected emission lines, as well as to purge obviously spurious detections (e.g. due to continuum residuals). Real detections were assigned with quality and confidence flags. Here, the quality flag encodes whether multiple emission lines of a source were detected (quality A), multiple emission lines are present but below the detection threshold (quality B), or whether the identification was based on a single line (quality C). By this definition all of the LAEs considered in the present analysis are quality C objects. As detailed in H017 (Sect. 3.1.4), the confidence values encode a more subjective measure of belief towards the final identification of a source, ranging from 1 (minor doubts) to 3 (no doubts). These values were assigned based on the apparent shape of the spectral profile and, if present, on the morphology and size of an optical counterpart in the HST images.

### 2.3. The Lyman $\alpha$ Emitter Sample

The final emission line catalogue published in H017 consists of 831 emission line galaxies, with 237 Ly $\alpha$  emitting galaxies in the redshift range  $2.97 \leq z \leq 5.99$ . Two of these high- $z$  galaxies exhibit clear signatures of active nuclei<sup>5</sup> and are also flagged as active galaxies in the Chandra 7Ms source catalogue (Luo et al. 2017). Another object was classified as a strong C iv emitter, and is therefore also likely not a star-forming LAE<sup>6</sup>. We note that these AGN are also the most luminous LAEs in our sample. In our analysis below we will discuss the effect of not excluding these *bona-fide* AGNs when determining the LAE LF.

All except five of the 234 non-AGN LAE galaxies have only a single line detected by LSDCat. The five exceptions are characterised by strongly pronounced double peaked Ly $\alpha$  profiles, with both peaks having individual entries in the emission line cata-

<sup>3</sup> LSDCat is publicly available via the Astrophysics Source Code Library: <http://ascl.net/1612.002> (Herenz & Wisotzki 2016).

<sup>4</sup> *QtClassify* is publicly available via the Astrophysics Source Code Library: <http://ascl.net/1703.011> (Kerutt 2017).

<sup>5</sup> MW IDs 104014050 and 115003085.

<sup>6</sup> MW ID 121033078.

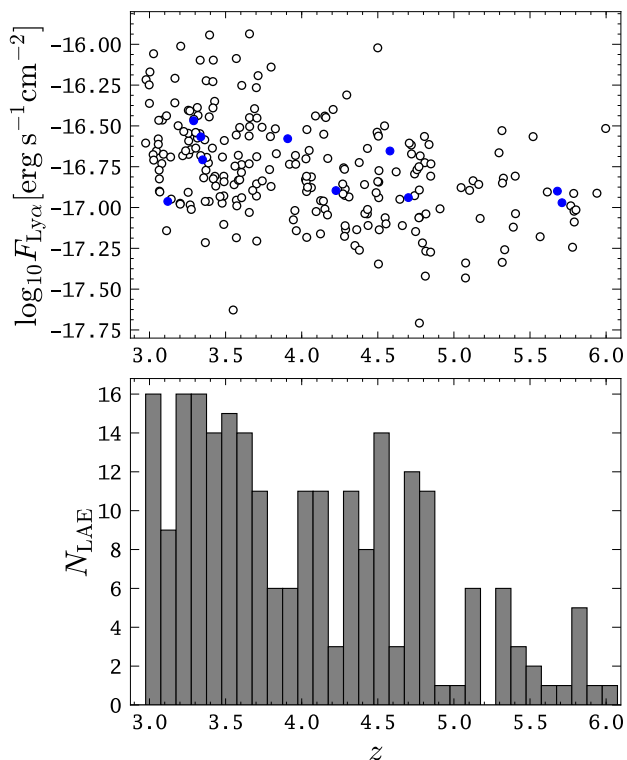


**Fig. 1.** *Top panel:* Fluxes and redshifts of the MW LAE sample used in this study (*open circles*) in comparison to the fluxes and redshifts of the MUSE HDFs LAEs used to determine a realistic selection function as described in Sect. 3.2 (*filled circles*). *Bottom panel:* Redshift histogram of the MW LAE sample (binning:  $\Delta z = 0.1$ ).

logue<sup>7</sup>. Moreover, only 20 sources have confidence value 1 assigned, i.e. there remained minor doubts on them being classified as Ly $\alpha$ . However, we found that excluding those low-confidence sources from our analysis had no impact on the resulting LF determinations.

LAE redshifts were determined by fitting the spectral profiles. As detailed in H017 we used the fitting formula

$$f(\lambda) = A \times \exp\left(-\frac{(\lambda - \lambda_0)^2}{2 \times (a_{\text{asym}}(\lambda - \lambda_0) + d)^2}\right) \quad (2)$$

introduced by Shibuya et al. (2014) to adequately model the asymmetric spectral profiles of LAEs. The free parameters  $A$ ,  $\lambda_0$ ,  $a_{\text{asym}}$ , and  $d$  in Eq. (2) are the amplitude, the peak wavelength, the asymmetry parameter, and the typical width of the line, respectively.

Emission line fluxes  $F_{\text{line}}$  of the LAEs were determined with the automated flux extraction routine of LSDCat. In Herenz & Wisotzki (2017) we found that for LAEs in the MW survey the automatic measurements from the software compare best to a manual curve-of-growth analysis over the spectral and spatial extent of the emitters when aperture radii of three times the Kron-radius (Kron 1980) were used. Thus we use these  $F_{\text{line}}(3 \times R_{\text{Kron}})$  fluxes as the basis for our luminosity function analysis. The mean and median  $3 \times R_{\text{Kron}}$  radii in which fluxes were extracted are  $2.1''$  and  $2.0''$ , respectively, with values ranging from  $1.8''$  to  $3.7''$ . However, we cautioned in H017 that quite frequently the spectral window of the automated flux extraction did not completely encompass the whole spectral profile of the LAEs.

<sup>7</sup> MW IDs 106014046, 115005089, 110003005, 122021111, and 123018120.

These profiles are often characterised by a weak secondary bump bluewards of the main spectral peak. This may result in flux-losses. In order to correct for those losses, we first visually inspected all spectral profiles to classify them as single or double peaked. We found that 90 LAEs in our sample show a weaker secondary blue peak. We then fitted all double peaked profiles with a linear combination of two profiles described by Eq. (2). From these fits we calculated the fraction of the line flux outside the spectral extraction window as flux correction factor. The average (median) flux correction factor for the double peaked emitters derived from this procedure is 1.17 (1.16). Using the single component fits of Eq. (2) we also derived flux correction factors for the single peaked LAE profiles. Here the correction factors are significantly smaller (mean: 1.03, median: 1.02), thus indicating the overall robustness of the automated procedure for simple emission line profiles. The final LAE fluxes used in our analysis are then obtained by multiplying the catalogued  $F_{\text{line}}(3 \times R_{\text{Kron}})$  fluxes by each individually determined correction factor. An overview of the fluxes and redshifts and a redshift histogram of the MW LAE sample are shown in Figure 1.

Finally, the measured fluxes are then converted into Ly $\alpha$  luminosities viz

$$L_{\text{Ly}\alpha} = 4\pi F_{\text{Ly}\alpha} D_L^2(z), \quad (3)$$

where  $D_L(z)$  is the luminosity distance corresponding to the redshift of the Ly $\alpha$  emitter that was determined from fitting the spectral line profile with Eq. (2).

### 3. The MUSE-Wide Lyman $\alpha$ emitter selection function

To derive the luminosity function from the MW LAE sample, we first need to determine the selection function for LAEs in our integral-field spectroscopic survey. The selection function encodes the probability  $f_C(F_{\text{Ly}\alpha}, \lambda)$  of observing a LAE with flux  $F_{\text{Ly}\alpha}$  at wavelength  $\lambda$  in our survey. Given an adopted cosmology it can also be uniquely represented in redshift-luminosity space:  $f_C(F_{\text{Ly}\alpha}, \lambda) \leftrightarrow f_C(L_{\text{Ly}\alpha}, z_{\text{Ly}\alpha})$ .

In order to construct  $f_C(F_{\text{Ly}\alpha}, \lambda)$  for MW, we study the success rate of recovering artificially implanted LAEs with our detection procedure. In Sect. 3.1 we perform this experiment with model sources characterised by a compact point-like spatial profile and a simple spectral profile. Then, in Sect. 3.2, we perform this experiment under more realistic assumptions by accounting for the observed variety in spectral- and spatial profiles of LAEs. To this aim we will make use of real LAEs observed in the MUSE HDFs (Bacon et al. 2015). Finally, we explain in Sect. 3.3 how the measured recovery fractions are converted to selection functions  $f_C(F_{\text{Ly}\alpha}, \lambda)$ .

#### 3.1. Source recovery experiment with artificial point sources

We first computed recovery fractions for an over-simplified case where we assumed that LAEs are perfect point sources with simple spectral profiles. In particular we modelled the light profiles of the implanted sources with a Moffat function (Moffat 1969). This parameterisation provides a reasonably good approximation of the seeing induced point-spread function in ground based optical to near-infrared observations (Trujillo et al. 2001). To account for the wavelength dependence of the full width at half maximum (FWHM) of the point spread function, we used the coefficients of linear fits of  $\text{FWHM}(\lambda)$  provided in Table 2 of

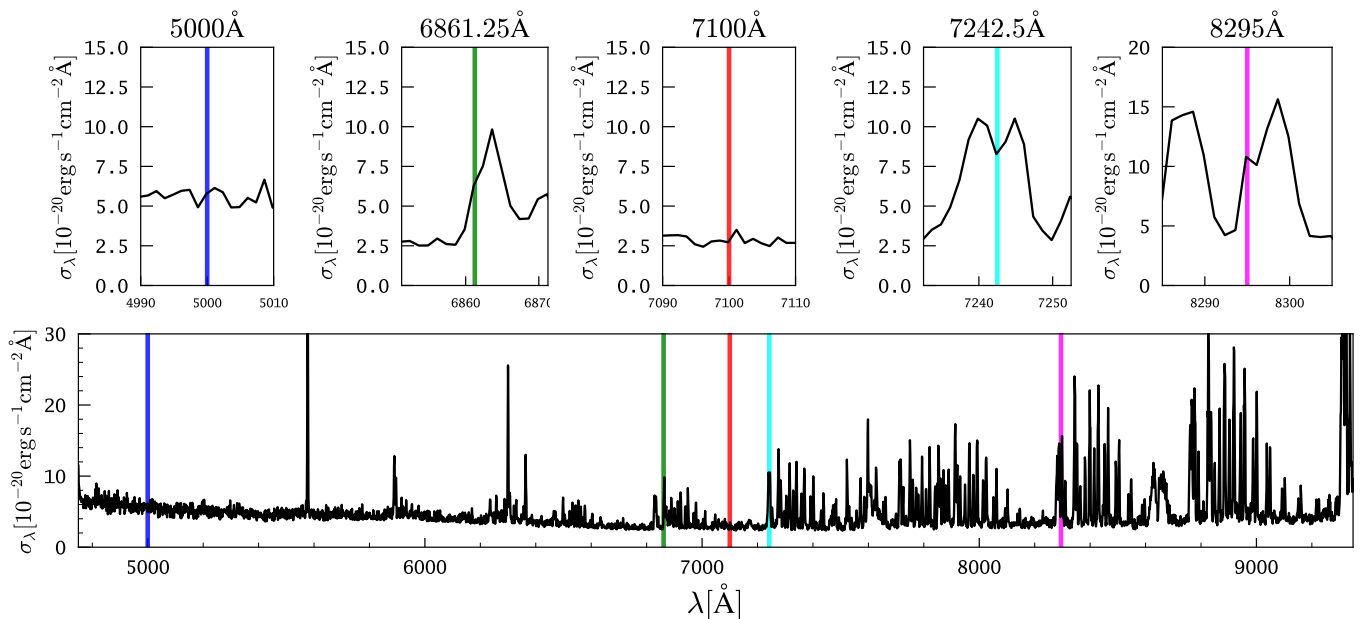


**Fig. 2.** Insertion wavelengths for completeness function estimation. The bottom panel shows the background noise over the whole spectral range, with vertical lines indicate the positions of the artificially implanted LAEs. The top panels are zoomed-in versions around the regions of interest. The colours of the vertical lines correspond to the colours used for the source recovery fractions in Figs. 3, 4, and 5.

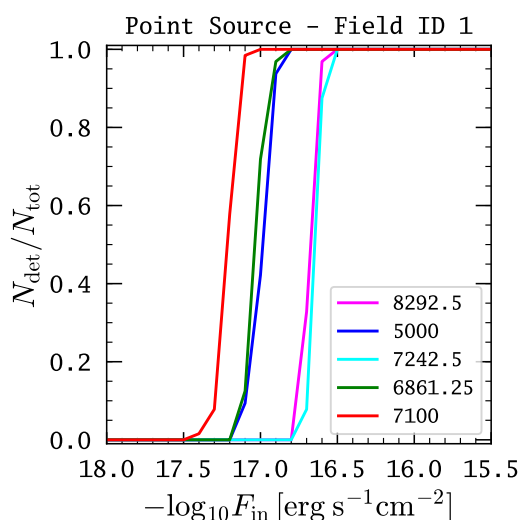


**Fig. 3.** Recovery fraction  $N_{\text{det}}/N_{\text{total}}$  from a source insertion and recovery experiment for simplified point-like emission sources at five different wavelengths (see Figure 2) in the MW pointing 01 datacube.  $N_{\text{total}} = 64$  is the number of inserted sources at a given flux level and  $N_{\text{det}}$  is the number of recovered sources for a given line flux  $F_{\text{in}}$  obtained with same detection procedure used to construct the original MW catalogue.

H017. The spectral profile of the fake sources is modelled as a simple Gaussian of 250 km s width (FWHM).

As it is computationally not feasible to perform the source insertion and recovery experiment for all wavelength layers in each of the 24 MW datacubes, we selected five insertion wavelengths that are representative of typical noise situations in the datacube (see Figure 2):  $\lambda_1 = 5000 \text{ \AA}$ ,  $\lambda_2 = 6861.25 \text{ \AA}$ ,  $\lambda_3 = 7100 \text{ \AA}$ ,  $\lambda_4 = 7242.5 \text{ \AA}$ , and  $\lambda_5 = 8292.5 \text{ \AA}$ . In particular, the spectral regions around 5000  $\text{\AA}$  and 7100  $\text{\AA}$  are typical regions devoid

of night sky line emission, while 6861.25  $\text{\AA}$  is in the wing of a sky line, and the 7242.5  $\text{\AA}$  and 8292.5  $\text{\AA}$  positions are chosen to be right between two neighbouring sky lines. At these insertion wavelengths we then populate each of the 24 MW cubes with  $N_{\text{tot}} = 64$  fake sources at different spatial positions. Instead of placing the inserted sources on a regular grid, we used a quasi-random grid based on a Sobol sequence (see e.g. Sect. 7.7 of Press et al. 1992). This is done to avoid placement of the sources at similar distances to the edges of the MUSE slice stacks. These stacks are arranged in a rectangular pattern, which is only slightly modulated by the small dither offsets during the observations. With this procedure we ensured that our selection function is not affected by systematic defects that are known to exist at the slice stack edges (see e.g. Fig. 3 in Bacon et al. 2017). We then inserted fake sources with 20 different flux levels from  $\log F_{\text{Ly}\alpha} [\text{erg s}^{-1} \text{cm}^{-2}] = -17.5$  to  $\log F_{\text{Ly}\alpha} [\text{erg s}^{-1} \text{cm}^{-2}] = -15.5$  in steps of 0.1 dex at the five chosen wavelength layers into each MW datacube. The  $20 \times 24 = 480$  datacubes were then continuum subtracted with the running median filter as described in Sect. 2.2. We then process these continuum subtracted cubes with LSDCat in the same way as for the original catalogue construction (Sect. 2.2). In order to decrease the computational cost for this experiment, we trimmed the continuum subtracted fake-source populated datacubes by  $\pm 30 \text{ \AA}$  around each insertion wavelength. For each subcube we then counted the number sources  $N_{\text{det}}$  that are recovered by LSDCat above the same detection threshold ( $S/N_{\text{det}} = 8$ ) that was used for the creation of the MW emission line source catalogue (cf. Sect. 2.2). As an example, we show in Fig. 3 the resulting recovery fractions for each insertion wavelength for MW pointing 01. We note that the shape and order of the curves is similar for all other pointings.

### 3.2. Source recovery experiment with real LAEs

We also performed a source insertion and recovery experiment using the 10 LAEs from the MUSE HDFS catalogue that have highest S/N-ratios (MUSE HDFS ID 43, 92, 95, 112, 139, 181,

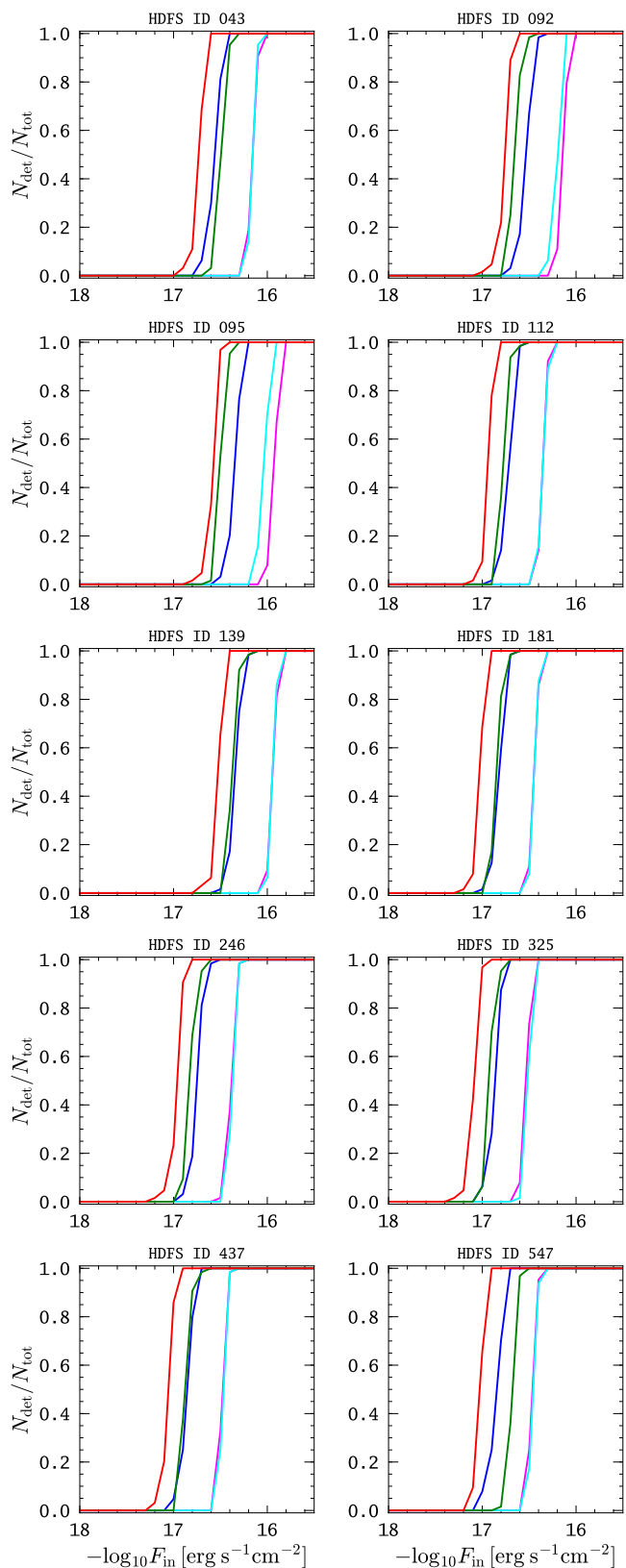


**Fig. 4.** Recovery fractions from a source insertion and recovery experiment with 10 MUSE HDFS LAEs for MW datacube 01. Each panel displays the recovery fraction  $N_{\text{det}}/N_{\text{total}}$  for a particular MUSE HDFS LAE of as a function of its scaled flux at 5 different wavelengths (see Figure 2). ( $N_{\text{total}}$  and  $N_{\text{det}}$  as defined in Figure 3).

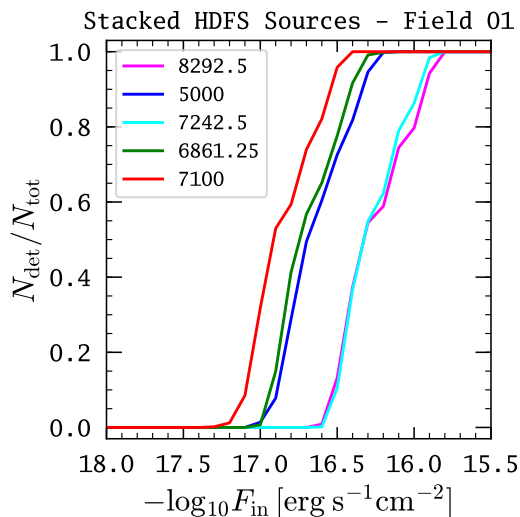


**Fig. 5.** Stack over the recovery fractions  $N_{\text{det}}/N_{\text{total}}$  of the 10 different MUSE HDFS LAEs used in the source recovery experiment. These curves represent the selection function at 5 different wavelengths in a MW datacube. Exemplarily, we show only the results for the MW datacubes 01, noting that the shape of the curves are similar for all other fields.

246, 325, 437, and 547 – all have  $S/N > 10$ ). These sources show a range of different surface-brightness profiles: E.g., while the LAEs 43, 92, and 95 are fairly extended, the LAEs 181, 325, and 542 show more compact surface brightness profiles (Wisotzki et al. 2016). They also represent a range in fluxes, redshifts and line profiles. Given their high  $S/N$ -ratios in the MUSE HDFS data, they are practically noise free compared to the noise level in MW, even when being multiplicatively rescaled to higher flux levels. We compare the fluxes and redshifts of these 10 LAEs to the actual MUSE-Wide sample in Figure 1. As evident, all MUSE HDFS LAEs used in the source insertion experiment could potentially be part of the MW Sample.

We now rescaled these LAEs to 20 different flux levels between  $\log F_{\text{Ly}\alpha} [\text{erg s}^{-1} \text{cm}^{-2}] = -17.5$  to  $\log F_{\text{Ly}\alpha} [\text{erg s}^{-1} \text{cm}^{-2}] = -15.5$  in steps of 0.1 dex (i.e. we use the same flux levels as for before for the simplified sources). For this purpose we first measured the fluxes from the MUSE HDFS LAEs by utilising LSDCat’s flux-measurement routine with circular apertures of radius  $3R_{\text{Kron}}$ . We then cut out mini cubes from the MUSE HDFS datacube that are centred on the LAEs. The vocals in those mini-cubes were then multiplied by constant factors to reach the desired flux levels. These  $20 \times 10$  (flux samples  $\times$  source samples) “fake-source” mini cubes were inserted into each of our 24 MW datacubes at the five different insertion wavelengths and at the same positions that were also used for the simplified sources.

When inserting the sources at different wavelengths we accounted for the redshift broadening of spectral profile, i.e. we kept the profile shape fixed in velocity space. We also needed to account for the differences in the points-spread functions between MW and MUSE HDFS. Since in all MW datacubes the point-spread function (PSF) is broader than the PSF in the HDFS, we have to degrade the PSF of the inserted mini cubes. To this aim we convolved their spatial layers with a 2D Gaussian of dispersion  $\sigma_{2D}(\lambda) = \sqrt{\sigma_{\text{MW}}(\lambda)^2 - \sigma_{\text{HDFS}}(\lambda)^2}$ , where  $\sigma_{\text{MW}}(\lambda)$  and  $\sigma_{\text{HDFS}}(\lambda)$  are the wavelength-dependent PSF dispersions of a MUSE-Wide datacube and the MUSE HDFS datacube, respec-

tively. Here the MUSE HDFS PSF was determined in a from fits to the brightest star in the field (see Fig. 2 of Bacon et al. 2015), while the linear model of H017 was used for the MW PSF.

After having continuum subtracted datacubes with artificially implanted sources, the next step is to perform the recovery experiment. To reduce the computational cost of this experiment, we trim the fake-source inserted cubes in wavelength range to  $\pm 30\text{\AA}$  around each insertion wavelength. The full recovery experiment is thus performed on  $20 \times 10 \times 5 \times 24 = 24000$  datacubes of dimensions  $\sim 300 \times 300 \times 50$  (neglecting empty edges due to the rotation of the MW pointings). Each of these cubes was processed with LSDCat using the same parameters that were used to generate the catalogue of LAEs in the 24 MW fields. We then counted the number of recovered sources  $N_{\text{det}}$  above the same detection threshold that was used in the creation of the MW LAE source catalogue ( $S/N_{\text{det}} = 8$ ).

We demonstrate the outcome of the recovery experiment with realistic LAES for the MW pointing 01 datacube in Figure 4, noting that the results for the other datacubes are similar: We found that the completeness curves for all emitters have a very steep cut-off at line fluxes of  $10^{-16} \dots 10^{-17} \text{ erg s}^{-1} \text{ cm}^{-2}$ . While for the more compact LAEs the cut-off is comparable to the one obtained for the idealised sources (cf. Figure 3), for the more extended LAEs it is significantly shifted to brighter flux levels. The exact turnover point on a given curve appears to be a complicated function of a source’s surface-brightness profile and its spectral profile. However, we observe that for a given source all curves are self-similar and the shift depends only on the insertion wavelength (Fig. 2). Since the 10 LAEs from the MUSE HDFS used in the recovery experiment are expected to be a representative subset of the overall high- $z$  LAE population, we expect the overall LAE selection function at a specific wavelength to be the average recovery fraction over all sources  $\langle N_{\text{det}}/N_{\text{tot}} \rangle$  at this wavelength. In Fig. 5 we show as an example these averaged recovery fractions for MW pointing 01. Similar to the idealised sources, the shape and the order of the curves is similar for all other pointings.

### 3.3. From recovery fractions to selection functions

Up to this point we are equipped with LAE selection functions for the MW LAEs only at 5 different wavelengths within the MUSE wavelength range. However, we notice in Figure 3 and Figure 5 that the curves at the different wavelengths are self-similar and that their order in flux is always the same. This result indicates that there is a universally shaped selection function whose shift with respect to the flux axis is determined by a wavelength dependent quantity. Indeed, we find that the shift of the 50% completeness point ( $f_C(F_{50}) = 0.5$ ) of the determined curves shows a nearly constant  $F_{50}/\tilde{\sigma}_{\text{emp}}$  ratio for all curves, with  $\tilde{\sigma}_{\text{emp}}$  being the empirically determined background noise convolved with a  $250 \text{ km s}^{-1}$  wide (FWHM) Gaussian. The ratio  $F_{50}/\tilde{\sigma}_{\text{emp}}(\lambda)$  is between 400 and 460 for the different datacubes; the exact value depends on the average datacube background noise and is a function of the observing conditions. Using this scaling we can compute  $f_{C,i}(F_{\text{Ly}\alpha}, \lambda)$  for each of the 24 MW pointings (here  $i$  indexes the pointing): We create a master  $f(F)$ -curve from shifting the 5 stacked curves on top of each other by requiring them to have the same  $f_C(F'_{50}) = 0.5$  value. For each wavelength bin we then shift this  $f(F)$ -master curve according to the  $F_{50}/\tilde{\sigma}_{\text{emp}}(\lambda)$ -proportionality to obtain  $f_{C,i}(F_{\text{Ly}\alpha}, \lambda)$ . The final selection functions for the MW LAE catalogue are then the average of all 24 selection functions.

The resulting selection function for the point-like emission line sources is called “point source selection function” (PSSF). This more realistic selection function is therefore called function “real source selection function” (RSSF). Both selection functions are shown in Figure 6 in redshift-flux space and in Figure 7 redshift-luminosity space.

The PSSF can be seen as a limiting depth of our survey, since it resembles closely the template of the matched filter used in the emission line source detection (H017). More importantly in comparison to the RSSF it also demonstrates the loss in sensitivity in LAE surveys due to the fact that these sources are not compact, but exhibit significant low surface brightness halo components. Moreover, while the transition from 0% to 100% completeness is quite rapid for the PSSF, the variety of Ly $\alpha$  halo properties encountered amongst LAEs leads to a much smoother transition. Notably, in extreme cases Ly $\alpha$  haloes can contain up to 90% of the total Ly $\alpha$  flux (Wisotzki et al. 2016; Leclercq et al. 2017). Therefore, the assumption of point-like LAEs in estimating the selection function leads to an overestimate of survey depth. While Grove et al. (2009) already noted this effect, they were not able to robustly quantify it due to the lack of deeper comparison data.

## 4. The Lyman $\alpha$ luminosity function – methods

Before presenting the results of the LAE LF in the next section, we provide here an overview of the methods used to derive the LAE LF in our integral field spectroscopic dataset.

We use three different non-parametric LF estimators, which are explained in Sect. 4.1: The “classical”  $1/V_{\text{max}}$ -method (Sect. 4.1.1), a binned alternative method to  $1/V_{\text{max}}$  introduced by Page & Carrera (Sect. 4.1.2), and the  $C^-$ -method (Sect. 4.1.3). As we will discuss, the latter two methods provide some advantages over the classical  $1/V_{\text{max}}$  approach. Moreover, we also make use of a non-parametric method to test the redshift evolution of the LAE LF (Sect. 4.1.4).

Furthermore, photometric uncertainties at low-completeness levels will lead to biases in the LF estimate. In order to avoid those biases we truncate the sample and define appropriate luminosity bins for the binned estimators. We motivate our truncation criterion and bin-size choice in Sect. 4.2.

Finally, in Sect. 4.3 we explain the maximum-likelihood fitting formalism that we employ to derive parametric models of the LAE LF.

### 4.1. Non-parametric luminosity function estimates

#### 4.1.1. The $1/V_{\text{max}}$ method

The first non-parametric LF estimator we consider is the so-called  $1/V_{\text{max}}$ -estimator (Schmidt 1968; Felten 1976) in a modified version to account for a complex, i.e. redshift- and luminosity-dependent, selection function (Fan et al. 2001; Caditz 2016).

The  $1/V_{\text{max}}$  estimator approximates the cumulative luminosity function

$$\Phi(L_{\text{Ly}\alpha}) = \int_{L_{\text{Ly}\alpha}}^{\infty} \phi(L'_{\text{Ly}\alpha}) dL'_{\text{Ly}\alpha}, \quad (4)$$

where  $\phi(L_{\text{Ly}\alpha})$  is the differential LF introduced in Eq. (1), via

$$\Phi(L_{\text{Ly}\alpha,k}) = \sum_{i \leq k} \frac{1}{V_{\text{max},i}}. \quad (5)$$

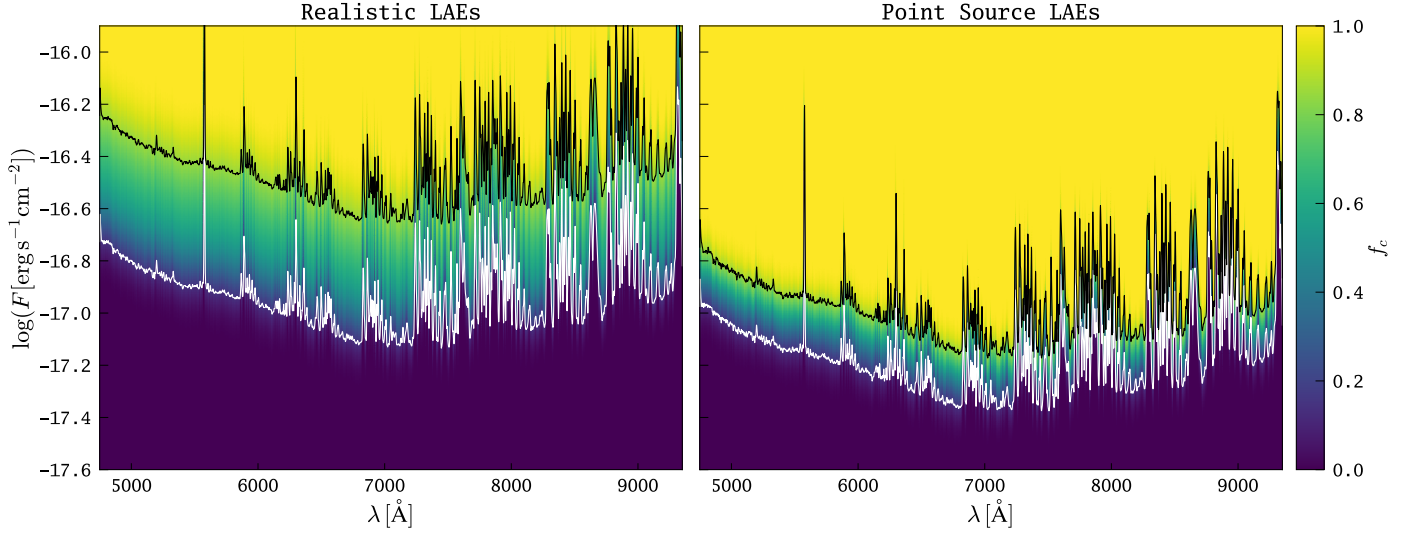


**Fig. 6.** Selection function  $f_c(F_{\text{Ly}\alpha}, \lambda)$  for LAEs in the MW survey. The white and black lines indicate the 15% and 85% completeness limits, respectively. The left panel shows the “real source selection function” (RSSF, see Sect. 3.2). The right panel shows the “point source selection function” (PSSF, see Sect. 3.1).

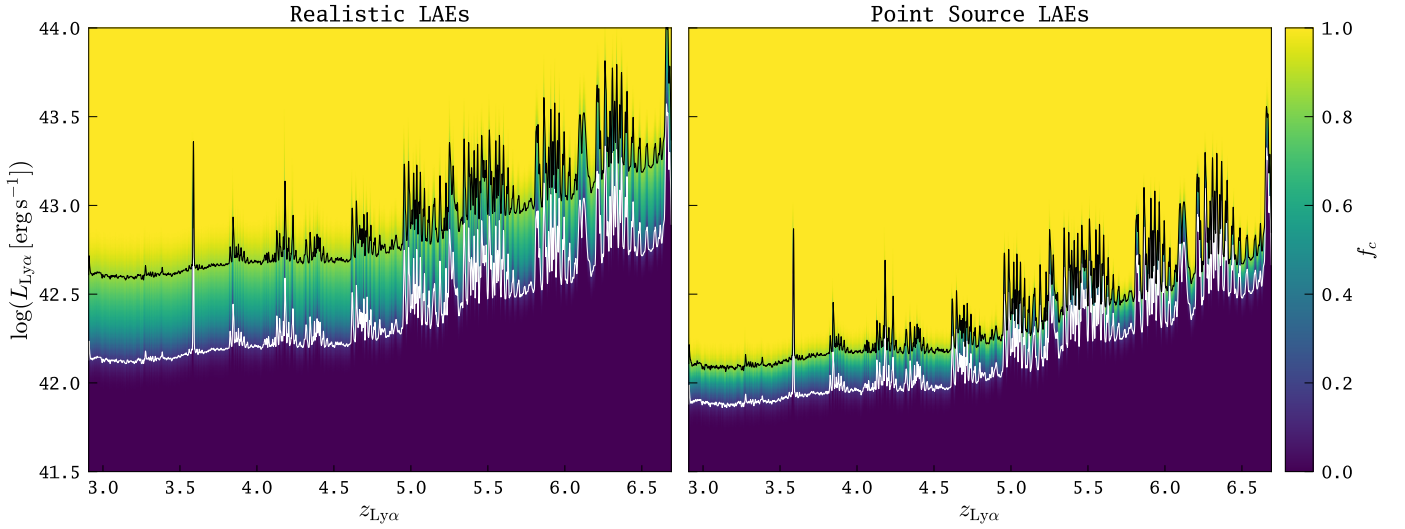


**Fig. 7.** Selection function for LAEs in the MW survey, similar to Figure 6, but now transformed to redshift-luminosity space.

Here, and in the following, we assume that the objects are ordered in  $\text{Ly}\alpha$  luminosity, i.e.

$$L_{\text{Ly}\alpha,1} > L_{\text{Ly}\alpha,2} > \dots > L_{\text{Ly}\alpha,N-1} > L_{\text{Ly}\alpha,N}. \quad (6)$$

$V_{\text{max},i}$  in Eq. (5) denotes the maximum volume accessible for each LAE  $i$  in the survey. In the presence of our redshift-dependent selection function  $f_c(L, z)$  (Fig. 7) we can write

$$V_{\text{max},i} = \omega \int_{z_{\text{min}}}^{z_{\text{max}}} f_c(L_{\text{Ly}\alpha,i}, z) \frac{dV}{dz} dz \quad (7)$$

(e.g. Wisotzki 1998; Johnston 2011). Here  $\omega$  is the angular area of the survey ( $\omega = 22.2 \text{ arcmin}^2$  for the 24 fields of the first instalment of the MW survey under consideration here),  $\frac{dV}{dz}$  is the differential cosmological volume element<sup>8</sup>, and  $z_{\text{min}}$  ( $z_{\text{max}}$ )

<sup>8</sup> For a definition of  $\frac{dV}{dz}$  see, e.g., Hogg (1999).

denotes the lower (upper) limit of the redshift range under consideration<sup>9</sup>.

Moreover, in the  $1/V_{\text{max}}$  formalism the differential LF can be approximated by the binned estimator

$$\phi_{1/V_{\text{max}}}(\langle L_{\text{Ly}\alpha} \rangle) = \frac{1}{\Delta L_{\text{Ly}\alpha}} \sum_k \frac{1}{V_{\text{max},k}}, \quad (8)$$

where  $\langle L_{\text{Ly}\alpha} \rangle$  is the average  $\text{Ly}\alpha$  luminosity of a bin,  $\Delta L_{\text{Ly}\alpha}$  is the width of the bin, and the sum runs over all sources  $k$  in that bin. The uncertainty for each bin is defined as

$$\Delta \phi_{1/V_{\text{max}}}(\langle L_{\text{Ly}\alpha} \rangle) = \sqrt{\frac{1}{\Delta L^2} \sum_i \frac{1}{V_{\text{max},i}^2}} \quad (9)$$

(e.g. Johnston 2011).

<sup>9</sup> In our study these limits are either imposed by the full spectral coverage of MUSE, i.e.  $(z_{\text{min}}, z_{\text{max}}) = (2.9, 6.7)$ , or by the redshift bins that we consider (see Table 1 below).

#### 4.1.2. The binned estimator proposed by Page & Carrera (2000)

The second non-parametric estimator we consider provides an alternative binned estimate for the differential LF. In its original form it was proposed by Page & Carrera (2000). Following Yuan & Wang (2013), who provide a thorough comparison with the  $1/V_{\max}$  method, we call it the  $\phi_{\text{PC}}$  estimator. This estimator was motivated by potential systematic biases in the  $1/V_{\max}$  estimator close to the flux limit of the survey. It has not yet been utilised to derive LAE LFs.

Instead of considering the maximum volume accessible for each individual source in the binned  $1/V_{\max}$ -estimator (Eq. 8), Page & Carrera (2000) argue that it is more robust to consider the average four-dimensional volume in redshift-luminosity space for each bin and then to divide the number of sources present in the bin by this hypervolume. In the presence of a redshift dependent selection function we can write the  $\phi_{\text{PC}}$  estimator as

$$\phi_{\text{PC}}(\langle L_{\text{Ly}\alpha} \rangle) = \frac{N}{\omega \int_{L_{\min}}^{L_{\max}} \int_{z_{\min}}^{z_{\max}} f_c(L_{\text{Ly}\alpha}, z) \frac{dV}{dz} dz dL}, \quad (10)$$

where again  $\langle L_{\text{Ly}\alpha} \rangle$  denotes the average Ly $\alpha$  luminosity of a bin,  $z_{\min}$  and  $z_{\max}$  are the limits of the redshift range under consideration,  $L_{\min}$  and  $L_{\max}$  are lower and upper bounds of the bin in which the LF is estimated, and  $N$  is the number of sources within the bin. In analogy to Eq. (9), we estimate the statistical uncertainty on  $\phi_{\text{PC}}(\langle L_{\text{Ly}\alpha} \rangle)$  by replacing  $N$  with  $\sqrt{N}$  in Eq. (10).

#### 4.1.3. The $C^-$ method

We also consider the  $C^-$  method for estimating the cumulative LF defined in Eq. 4. This method was introduced into the astronomical literature by Lynden-Bell (1971) and the generalisation for complex selection functions was introduced by Petrosian (1992). The generalised  $C^-$  method has, as of yet, not been used to derive LAE LFs. Formal derivations of the method in the presence of a redshift- and luminosity-dependent selection function are given elsewhere (e.g. Fan et al. 2001; Johnston 2011; Caditz 2016), here we just summarise the computational algorithm<sup>10</sup>.

The first step in the generalised  $C^-$  method is to define a so-called generalised comparable set  $J_i$  for each LAE  $i$  that contains all LAEs  $j$  with higher Ly $\alpha$  luminosity:

$$J_i = \{j : L_j > L_i\}. \quad (11)$$

The next step is to make a weighted count of the number of LAEs in each comparable set

$$T_i = \sum_{j=1}^{N_i} w_j, \quad (12)$$

where  $N_i$  is the number of LAEs in the comparable set  $J_i$ . The weights  $w_j$  for each object  $j$  in  $J_i$  are given by the selection probability if the  $J_i$ -defining object  $i$  with its Ly $\alpha$  luminosity  $L_{\text{Ly}\alpha,i}$  would have been detected at the redshift of an object  $j$ ,  $f_c(L_{\text{Ly}\alpha,i}, z_j)$ , normalised by  $j$ 's actual selection probability  $f_c(L_{\text{Ly}\alpha,j}, z_j)$ , i.e.

$$w_j = \frac{f_c(L_{\text{Ly}\alpha,i}, z_j)}{f_c(L_{\text{Ly}\alpha,j}, z_j)}. \quad (13)$$

<sup>10</sup> An introduction into the  $C^-$  method is also presented in Chapter 4.9.1. of the Ivezić et al. (2014) textbook.

Since by construction  $L_{\text{Ly}\alpha,j} > L_{\text{Ly}\alpha,i}$ , and since  $f_c$  is monotonically increasing with luminosity at a given redshift,  $w_j \leq 1$  holds. With these weighted counts then the cumulative LAE LF is given as

$$\Phi(L_{\text{Ly}\alpha,k}) = \Phi(L_{\text{Ly}\alpha,1}) \prod_{i=2}^k \left(1 + \frac{1}{T_i}\right). \quad (14)$$

where the normalisation  $\Phi(L_{\text{Ly}\alpha,1})$  has to be determined separately (see Sect. 4.1.4 below).

A potential advantage of the  $C^-$ -method over the  $1/V_{\max}$  method is that it only requires evaluation of the selection function at redshifts where sources were actually detected, whereas the calculation of the LF using the  $1/V_{\max}$ -method requires integration over the selection function over the whole redshift range of interest.

Caditz (2016) provides a detailed formal comparison between the  $C^-$  and  $1/V_{\max}$  estimators, showing that both are asymptotically unbiased, i.e. both  $1/V_{\max}$  and  $C^-$  yield a correct estimate of the true luminosity function for large number of objects and a correct estimate of the selection function. However, the main difference between the two estimators is that  $1/V_{\max}$  is more sensitive to uncertainties in the selection function, while  $C^-$  is more sensitive to random fluctuations in the sample.

#### 4.1.4. A non-parametric test for LF evolution

The  $1/V_{\max}$ -method as formulated in Sect. 4.1.1 explicitly assumes that the LF is non-evolving over the redshift range under consideration, whereas the key assumption in the above described  $C^-$ -method is that the distribution function  $\Psi(L, z)$ , describing a potentially evolving LF as a scalar field in redshift-luminosity space, is separable, i.e.

$$\psi(L, z) = \rho(z)\phi(L). \quad (15)$$

Here  $\rho(z)$  describes the mean density of sources as a function of redshift. Thus, if Eq. (15) is an adequate description of the evolving LF, then  $\phi(L)$ , and correspondingly  $\Phi(L)$ , would retain its shape over the redshift range under consideration, with only the overall normalisation being allowed to change.

The assumption of an LF evolving according to Eq. (15) is commonly referred to as pure density evolution. In principle  $\rho(z)$  can also be determined with the formalism described above, by just exchanging redshifts with luminosities of object  $i$  in Eq. (12) and then using Eq. (14) to estimate  $\rho(z)$ . While such a derivation could be used to normalise the cumulative LF from the  $C^-$ -method, we here take the short-cut by utilising  $\Phi(L_{\text{Ly}\alpha,1})$  from the  $1/V_{\max}$  method in Eq. (14),

$$\Phi(L_{\text{Ly}\alpha,1}) = \frac{1}{V_{\max,1}}, \quad (16)$$

i.e. we implicitly assume that  $\rho$  is constant over the redshift ranges under consideration.

Following Fan et al. (2001), we test the validity of the pure density evolution of the LAE LF in the luminosity range probed by our survey with the statistical test developed by Efron & Petrosian (1992). Therefore we calculate for each  $J_i$  the generalised rank  $R_i$  of  $z_i$ :

$$R_i = \sum_{j=1}^{N_i} w_j \Theta(z_i - z_j), \quad \text{with } \Theta(x) = \begin{cases} 0 & \text{for } x < 0 \\ 1 & \text{for } x \geq 0 \end{cases}. \quad (17)$$

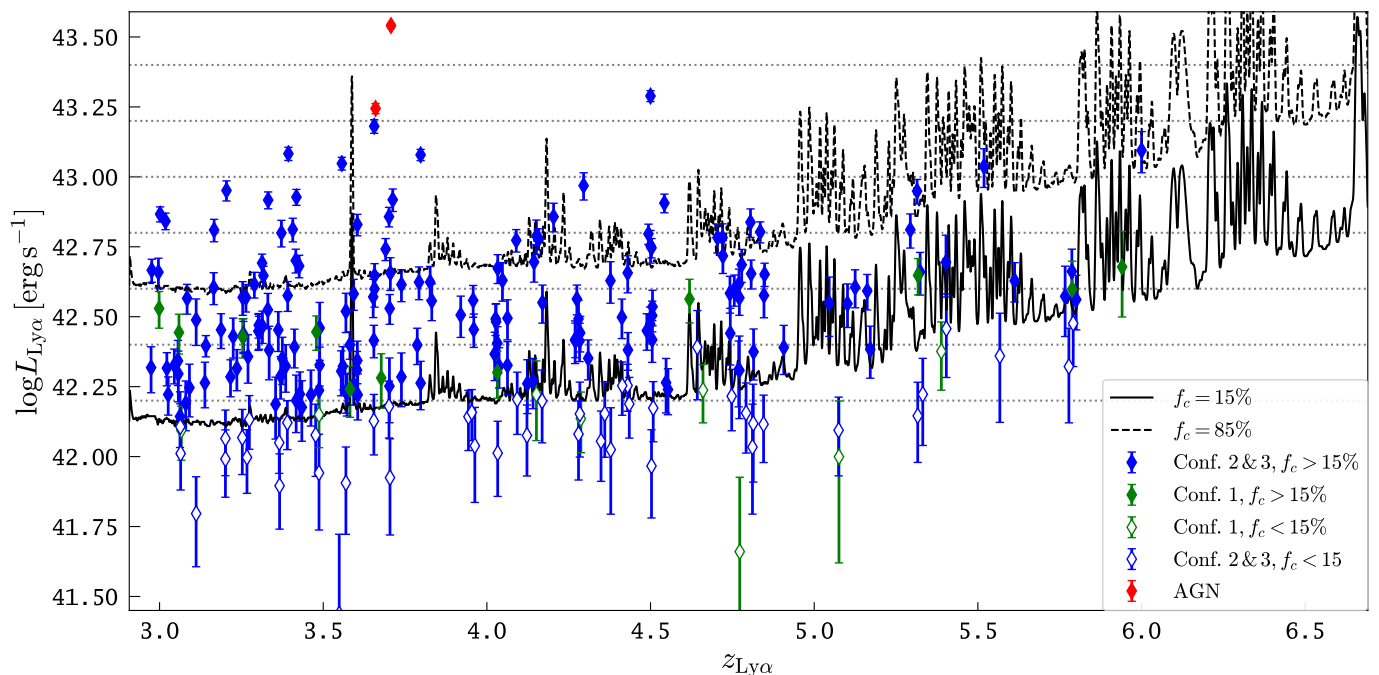


**Fig. 8.** LAE sample of the first 24 MW pointings in redshift-luminosity space. The dashed line represents the 85% RSSF completeness limit, while the black line denotes the 15% RSSF completeness limit, at which we truncate our sample. 179 of 237 (75.6%) LAEs remain in the truncated sample. Individual emitters are colour coded according to their assigned confidence flags (blue — little to no doubts on being an LAE; green — LAEs flagged as uncertain; more details on how the confidence values were assigned are given in Sect. 3.2 of H017). The two highest  $L_{Ly\alpha}$  objects are AGN indicated by red symbols. Sources below the truncation line are shown with open symbols. Horizontal dotted lines denote the adopted bin boundaries ( $\log L_{Ly\alpha,bin}[\text{erg s}^{-1}] = 42.2 + i \times 0.2$  for  $i = 0, 1, \dots, 5$ ) for the binned LAE LF estimates.

If  $z$  is independent of  $L$  in the sense of Eq. (15), then the  $R_i$ 's should be distributed uniformly between 0 and the corresponding  $T_i$ 's, i.e. the expectation value of  $R_i$  is  $E_i = T_i/2$  and its variance is  $V_i = T_i^2/12$ . Moreover, then the statistic

$$\tau = \frac{\sum_i (R_i - E_i)}{\sqrt{\sum_i V_i}} \quad (18)$$

is approximately a standard normal distribution under the null hypothesis that independence between  $z$  and  $L$  in Eq. (15) is valid.

We follow the literature by adopting  $|\tau| < 1$  as the critical value at which the independence assumption cannot be rejected (Efron & Petrosian 1992; Fan et al. 2001). We point out that for a standard normal distribution this value corresponds to p-values  $p_0 > 0.16$ , i.e. it is decidedly larger than commonly adopted significance levels to reject the null hypothesis (e.g.,  $p_0 < 0.05$  for  $1\sigma$ ).

#### 4.2. Truncation and Binning of the Sample

Non-parametric estimates of the differential luminosity function, regardless of the utilised estimator, require binning of the sample in luminosities. Moreover, at the faintest luminosities the photometric uncertainties become so large that they would translate into a large uncertainties for the completeness correction in the LF estimation. This potential bias can be avoided by trimming the sample from such sources. We visualise our choice of bin sizes and truncation limit for the RSSF in Figure 8.

We curtail the sample from sources that are detected below the  $f_c = 0.15$  completeness limit. As can be seen in Figure 8, the vast majority of LAEs below the  $f_c = 0.15$  limit have photometric errors that extend below the 0% completeness line, which

provides the main motivation for this truncation limit. This truncation limit removes 54 LAEs from the initial MW LAE sample for the RSSF. In the calculation of the luminosity function, we account for the truncation limit by setting  $f_c \equiv 0$  for all  $f_c < 0.15$ .

We chose our lowest luminosity boundary to be  $\log L_{Ly\alpha}[\text{erg s}^{-1}] = 42.2$ . We motivate this value by the fact that it straddles our RSSF truncation criterion in the  $z \lesssim 5$  region in the sample (Figure 8). However, as we opt for an integer single digit, this removes four additional objects from the LF sample truncated according to the RSSF. For the PSSF all except one source have  $f_c > 0.15$  above  $\log L_{Ly\alpha}[\text{erg s}^{-1}] = 42.2$ . We motivate our adopted bin-size  $\Delta \log L_{Ly\alpha}[\text{erg s}^{-1}] = 0.2$  by being significantly larger than the photometric error in the lowest luminosity bin. Moreover, we will show in Sect. 5.2 that for this bin-size the non-parametric estimates are in optimal agreement with the parametric maximum-likelihood solution.

Although estimating the binned differential LF is popular in the literature, we point out that binning represents a loss of information<sup>11</sup>, while all information present in the source catalogue is retained when deriving the cumulative LF (Felten 1976; Cadriz 2016). Moreover, the adopted maximum-likelihood procedure explained in the next section does not require binning of the data. We here use the binned estimates only for visual comparison to the binned values from the literature in combination with our derived Schechter parameterisation (Sect. 7 below).

<sup>11</sup> A recent discussion of the pitfalls when utilising binning in the analysis of astronomical data was presented in Steinhardt & Jermyn (2018).

### 4.3. Parametric maximum likelihood luminosity function estimation

In order to obtain a parametric description of the MW LAE LF we use the maximum likelihood parameter estimation approach introduced by Sandage et al. (1979) into the field of observational cosmology. Maximum likelihood estimation is a statistical technique to estimate the parameters of a model given the data. We therefore need to assume an analytical expression for the LF. The Schechter function (Schechter 1976) is the most commonly adopted functional form for the Ly $\alpha$  LF:

$$\phi(L) dL = \phi^* \left( \frac{L}{L^*} \right)^\alpha \exp\left(-\frac{L}{L^*}\right) \frac{dL}{L^*}. \quad (19)$$

We obtain the free parameters  $L^*$  (characteristic luminosity in  $\text{erg s}^{-1}$ ),  $\alpha$  (faint-end slope) and  $\phi^*$  (normalisation in  $\text{Mpc}^{-3}$ ) by maximising the likelihood function

$$\mathcal{L} = \prod_{i=1}^{N_{\text{LAE}}} p(L_i, z_i), \quad (20)$$

where

$$p(L_i, z_i) = \frac{\phi(L_i) f_c(L_i, z_i)}{\int_{L_{\min}}^{L_{\max}} \int_{z_{\min}}^{z_{\max}} \phi(L) f_c(L, z) \frac{dV}{dz} dL dz} \quad (21)$$

(e.g. Sandage et al. 1979; Fan et al. 2001; Johnston 2011). In practice we search for the minimum of

$$S = -2 \times \ln \mathcal{L}. \quad (22)$$

Evaluation of this equation thus requires a summation over the entire unbinned sample. As can be seen in Eq. 21, the space density scaling factor  $\phi^*$  cancels out and is thus not really a free parameter in the fitting process. For any given combination of  $L^*$  and  $\alpha$  the value of  $\phi^*$  is however uniquely determined since the integral in the denominator must equal the total number of objects in the sample used to calculate the likelihood function (e.g., Mehta et al. 2015).

Even simpler than a Schechter function is a power-law distribution of

$$\phi(L) dL = \frac{\phi^*}{L^*} \times L^\beta dL, \quad (23)$$

which lacks the exponential cutoff and thus implies a larger fraction of high-luminosity objects for equal power law indices  $\beta = \alpha$ . Comparing Eq. (23) to Eq. (21) it becomes evident that only  $\beta$  is a free parameter in the likelihood function, but similar as above, the ratio  $\phi^*/L^*$  is uniquely constrained by the total number of objects.

We do not consider more complex parametric expressions for the Ly $\alpha$  LF such as a double power law because, as demonstrated below (Sect. 5.2), these are not required for our data.

## 5. The Lyman $\alpha$ luminosity function – Results

### 5.1. Non-parametric reconstructions of the LAE LF

We first employ the non-parametric statistical test described in Sect. 4.1.4 to investigate whether the observed MW LAE LF is consistent with a pure density evolution scenario. Table 1 lists the obtained  $\tau$ -values from Eq. (18) along with the corresponding  $p$ -values under the normal distribution approximation. We calculated  $\tau$  both for the RSSF and the PSFF. Moreover, we not only tested evolution for the full MW redshift range, but also

**Table 1.** Results of statistical test according to Eq. (18) for testing the assumption of pure density evolution as defined in Eq. (15).

Redshift range	$ \tau_{\text{PSSF}} $	$ \tau_{\text{RSSF}} $	$p_{\text{PSSF}}$	$p_{\text{RSSF}}$
$2.9 < z \leq 4$	0.47	0.24	0.32	0.40
$4.0 < z \leq 5.0$	0.79	0.98	0.21	0.16
$5.0 < z \leq 6.7$	0.05	0.29	0.48	0.39
$2.9 < z \leq 6.7$	0.46	0.31	0.32	0.38

**Notes.**  $\tau$  values were computed for the point source selection function ( $\tau_{\text{PSSF}}$ ) and the selection function accounting for extended Ly $\alpha$  emission ( $\tau_{\text{RSSF}}$ ). The corresponding values of  $p$  for a standard normal distribution are given in the third and fourth column.

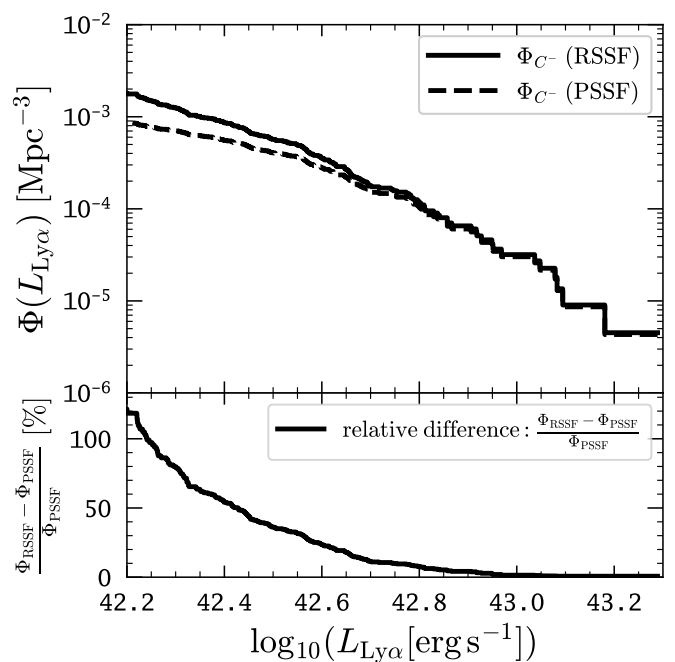


**Fig. 9.** *Top panel:* Global ( $2.9 \leq z \leq 6.7$ ) cumulative LAE LF from MW obtained with the  $C^-$ -method utilising the realistic source selection function (RSSF) and point-source selection function (PSSF). *Bottom panel:* Relative difference in per-cent between cumulative LFs utilising the RSSF and PSSF.

within three redshift ranges:  $2.9 < z \leq 4$ ,  $4 < z \leq 5$ , and  $5 < z \leq 6.7$ . Regardless of the adopted selection function, we find that the pure density evolution scenario cannot be rejected over the full redshift range (i.e.  $|\tau| < 1$ , thus  $p_0 > 0.16$ ), as well as in the redshift ranges. This means that over the dynamic range of probed Ly $\alpha$  luminosities the shape of the observed LAE LF remains unchanged at  $3 \lesssim z \lesssim 5$ . The test, however, is not sensitive for a possible change in the normalisation. But, we will demonstrate below (see especially Figure 19) that such a change in normalisation is also not required for the observed LAE LF.

A non-evolving apparent LAE LF is consistent with the result from the NB imaging survey by Ouchi et al. (2008). This study found no significant differences between the apparent (i.e. uncorrected for Ly $\alpha$  absorption by the intergalactic medium) LAE LF in their three surveyed redshift slices ( $z \approx \{3.1, 3.7, 5.7\}$ ). On the other hand, at first our result appears to be in tension with the recently reported LAE LF evolution from  $z \approx 2.5$  to  $z \approx 6$  within the SC4K survey (Sobral

**Table 2.** Binned differential LAE LF from the first 24 MW pointings.

$\log L_{\text{Ly}\alpha}$ ( $\text{erg s}^{-1}$ )	$N_{\text{LAE}}$	$\phi_{\text{PC}}$ ( $\text{Mpc}^{-3}[\Delta \log L_{\text{Ly}\alpha}]^{-1}$ )	$\Delta\phi_{\text{PC}}$ ( $\text{Mpc}^{-3}[\Delta \log L_{\text{Ly}\alpha}]^{-1}$ )	$\phi_{1/V_{\text{max}}}$ ( $\text{Mpc}^{-3}[\Delta \log L_{\text{Ly}\alpha}]^{-1}$ )	$\Delta\phi_{1/V_{\text{max}}}$ ( $\text{Mpc}^{-3}[\Delta \log L_{\text{Ly}\alpha}]^{-1}$ )
42.3	52	$5.5 \times 10^{-3}$	$7.7 \times 10^{-4}$	$5.9 \times 10^{-3}$	$8.6 \times 10^{-4}$
42.5	59	$3.0 \times 10^{-3}$	$4.0 \times 10^{-4}$	$3.1 \times 10^{-3}$	$4.1 \times 10^{-4}$
42.7	40	$1.4 \times 10^{-3}$	$2.2 \times 10^{-4}$	$1.4 \times 10^{-3}$	$2.3 \times 10^{-4}$
42.9	17	$4.7 \times 10^{-4}$	$1.1 \times 10^{-4}$	$4.8 \times 10^{-4}$	$1.2 \times 10^{-4}$
43.1	6	$1.4 \times 10^{-4}$	$5.8 \times 10^{-5}$	$1.5 \times 10^{-4}$	$5.9 \times 10^{-5}$
43.3	1	$2.3 \times 10^{-5}$	$2.3 \times 10^{-5}$	$2.3 \times 10^{-5}$	$2.3 \times 10^{-5}$

**Notes.**  $\phi_{\text{PC}}$  is computed with the Page & Carrera (2000) estimator (Sect. 4.1.2), while  $\phi_{1/V_{\text{max}}}$  results from binned  $1/V_{\text{max}}$  estimator (Sect. 4.1.1).

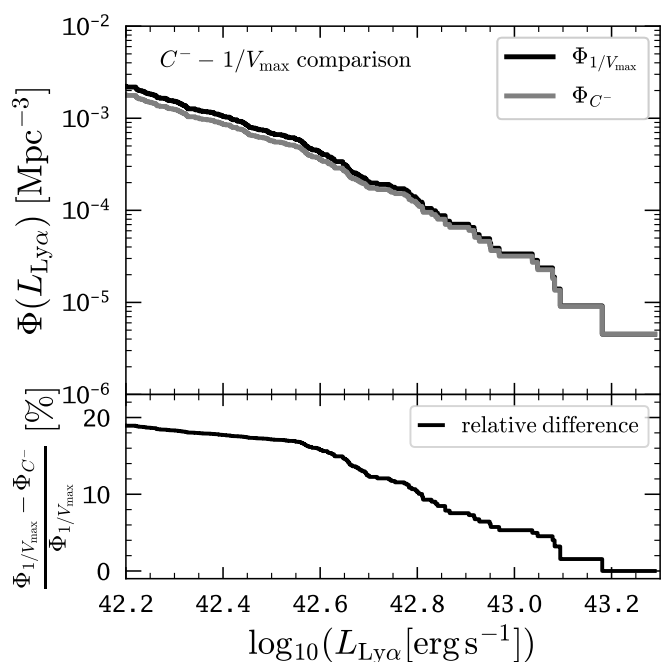


**Fig. 10.** Comparison of the RSSF completeness corrected cumulative LAE LFs obtained with the  $C^-$  and  $1/V_{\text{max}}$  estimators. *Top panel:* Cumulative LAE LFs from both methods. *Bottom panel:* Relative difference in per-cent between  $1/V_{\text{max}}$  and  $C^-$  method.

et al. 2018b). But, the change in the SC4K LAE LFs is driven by a decreasing number density of the highest luminosity LAEs ( $\log L_{\text{Ly}\alpha}[\text{erg s}^{-1}] \gtrsim 43.0$ ). Unfortunately, with the current MW data we do not sample a large enough number of such luminous LAEs to obtain a statistically robust confirmation of this result. Moreover, the current MW sample is also not well populated with  $z \gtrsim 5.5$  LAEs. Thus, as of yet, we also can not add constraints to the ongoing debate in the literature regarding a possible LAE LF evolution between  $z = 5.7$  and  $z = 6.6$  (Ouchi et al. 2010; Santos et al. 2016; Konno et al. 2018).

We now analyse the differences in the resulting LAE LF when employing the two different selection functions constructed in Sect. 3. To this aim we plot in Figure 9 the resulting cumulative LAE LFs obtained with the  $C^-$ -method (Sect. 4.1.3) for the RSSF, which explicitly accounts for the extended low-surface brightness haloes of LAEs (left panel in Figure 6), and for the PSSF, which assumes LAEs to be compact PSF broadened sources (right panel in Figure 6 and 7). We find that at the faint-end of our probed luminosity range ( $\log L_{\text{Ly}\alpha}[\text{erg s}^{-1}] =$

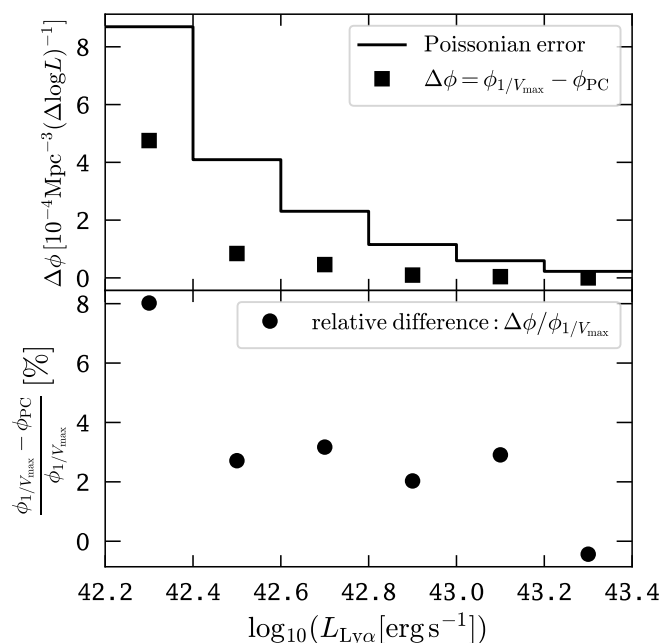


**Fig. 11.** *Top panel:* Absolute difference between binned  $1/V_{\text{max}}$  and  $\phi_{\text{PC}}$  estimator for global MW LAE LF in comparison to the Poissonian errors in each bin. *Bottom panel:* Relative difference between the two binned estimators in per-cent.

42.2) the inferred LAE density utilising the RSSF is a factor of 2.5 higher compared to the PSSF:  $\Phi_{\text{RSSF}}(\log L_{\text{Ly}\alpha}[\text{erg s}^{-1}] = 42.2) = 2 \times 10^{-3} \text{ Mpc}^{-3}$ , while  $\Phi_{\text{PSSF}}(\log L_{\text{Ly}\alpha}[\text{erg s}^{-1}] = 42.2) = 8 \times 10^{-4} \text{ Mpc}^{-3}$ .

We argue that due to the ubiquity of extended Ly $\alpha$  emission around LAEs, the RSSF represents a more realistic selection function. Hence, we regard the LAE LF constructed with this completeness correction as unbiased. Since previous LAE LF determinations, except Drake et al. (2017a), have not accounted for extended nature of LAEs in their selection functions, we expect similar biases in their inferred number densities close to their limiting luminosities. Indeed, we will demonstrate in Sect. 6 that our PSSF completeness-corrected Ly $\alpha$  LF agrees better with most literature estimates. Therefore, we emphasise that our PSSF LAE LF estimates here only serve demonstrative purposes, while the RSSF corrected estimate can be regarded as our best estimate.

Numerically, we obtain the same difference between the LAE LFs from the different selection functions when utilising

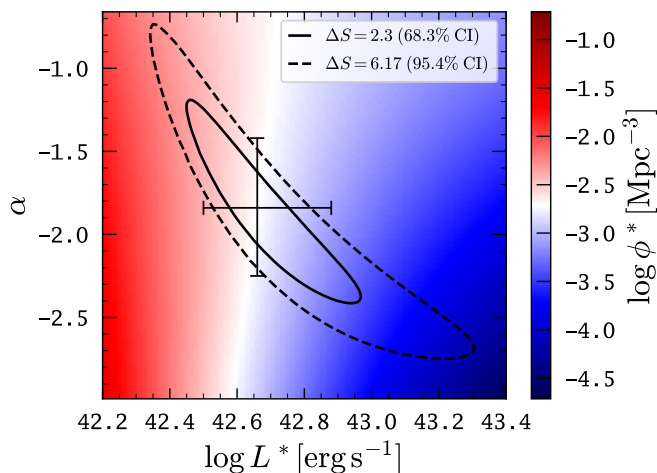


**Fig. 12.** Results from the Schechter function ML fit for the global MW LAE LF. Contours are drawn at  $\Delta S = \{2.3, 6.17\}$  thereby outlining the {68.3%, 95.4%} confidence intervals for  $\alpha$  and  $\log L^*$ . In colour we show the normalisation  $\log \phi^*$ , which is a dependent quantity on  $\alpha$  and  $L^*$ , i.e. it is not a free parameter in the fitting procedure. The cross indicates the best fitting  $(\log L^*[\text{erg s}^{-1}], \alpha) = (42.66, -1.84)$ . At this point in  $\log L^* - \alpha$  space the dependent normalisation is  $\log \phi^*(\log L^*, \alpha)[\text{Mpc}^{-3}] = -2.71$ . The 1D error-bars show the 68.3% confidence interval from the marginalised distribution in  $\alpha$  and  $\log L^*$  (see text).

the  $1/V_{\text{max}}$  estimator (Sect. 4.1.1). To demonstrate the similarity in the resulting LFs between  $C^-$  and  $1/V_{\text{max}}$  we compare in Figure 10 the inferred cumulative LAE LFs from both estimators. The maximum discrepancy occurs at the faint-end of our probed luminosity range. Here  $1/V_{\text{max}}$  provides slightly higher LAE densities than  $C^-$ :  $\Phi_{1/V_{\text{max}}}(\log L_{\text{Ly}\alpha}[\text{erg s}^{-1}] = 42.2) = 1.2 \times \Phi_{C^-}(\log L_{\text{Ly}\alpha}[\text{erg s}^{-1}] = 42.2)$ . The same result is obtained for the PSSF. As outlined in Sect. 4.1.3, while the  $C^-$  construction requires only an evaluation of the selection function at redshifts where objects are detected, the  $1/V_{\text{max}}$  estimate requires the evaluation of an integral over the selection function at all redshifts. Since our selection function stems from an extrapolation of the results from a source insertion and recovery experiment at five discrete wavelengths, the two estimators deal differently with possible uncertainties from this extrapolation approach. Encouragingly, the differences in the final LAE LF result are small. This validates the robustness of our selection function construction.

Lastly, we compute binned estimates from our sample using the bins motivated in Sect. 4.2 with the  $1/V_{\text{max}}$  (Sect. 4.1.1) and  $\phi_{\text{PC}}$  (Sect. 4.1.2) estimators. The results are given in Table 2. In Figure 11 we compare the results from the two different estimators. Following the expectation of Page & Carrera (2000), the binned  $1/V_{\text{max}}$  estimator is biased to higher values of the differential LF, especially in the low-luminosity bins near the completeness limit. We find the maximum discrepancy in the lowest luminosity bin to be 8%. However, at the current size of the MW sample the results are within the statistical counting error for each bin. Nevertheless, we encourage the use of the Page & Carrera (2000) estimator in future constructions of the binned LAE LF with larger samples, since it is less biased compared to the classical  $1/V_{\text{max}}$  techniques in the lowest luminosity bins of the sample (see also Yuan & Wang 2013).

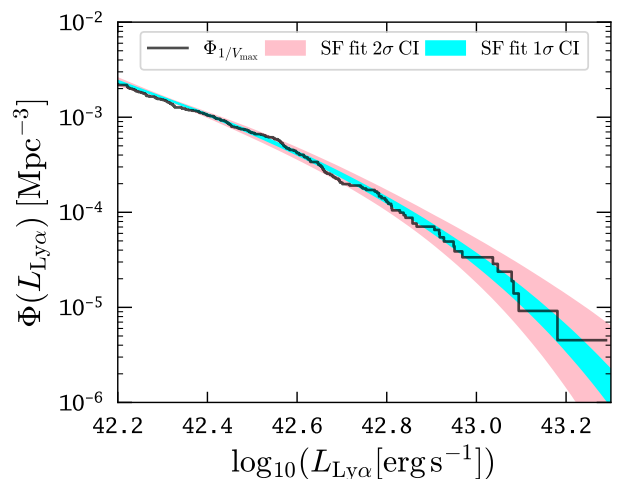


**Fig. 13.** Cumulative LAE LF from MW obtained with the  $1/V_{\text{max}}$  estimator in comparison to 68.3% and 95.4% confidence limits of the ML Schechter fit.

## 5.2. Parametric modelling

In order to obtain a parametric form of the LAE LF we evaluate the inverted log-likelihood function in Eq. (22) “brute-force” for a densely sampled grid of the Schechter function (Eq. 19) parameters  $L^*$  and  $\alpha$ . The minimum of Eq. (22) function represents the maximum-likelihood solution. It is found for  $\log L^*[\text{erg s}^{-1}] = 42.66$  and  $\alpha = -1.84$ . The corresponding value for the normalisation  $\phi^*$  is  $\log \phi^*[\text{Mpc}^{-3}] = -2.71$ . In Figure 12 the  $\Delta S = 2.3$ , and  $\Delta S = 6.17$  contours from the evaluation of Eq. (22) are shown. These two contours correspond to the standard  $1\sigma$  and  $2\sigma$  confidence (68.3% and 95.4%) regions. In this figure we also visualise the dependence of the normalisation  $\phi^*$  on  $L^*$  and  $\alpha$ .

From the “banana-shaped” appearance of the  $\Delta S$  contours in Figure 12 it is evident that we have a strong degeneracy between  $L^*$  and  $\alpha$ : Higher  $L^*$  values require steeper faint end slopes, i.e. smaller  $\alpha$ ’s, and vice-versa. By marginalising over  $\alpha$  and  $L^*$  we recover the 1D 68.3% confidence intervals  $\log L^*[\text{erg s}^{-1}] = \{42.72^{+0.23}_{-0.97}, 42.74^{+\infty}_{-0.19}, 42.66^{+0.42}_{-0.19}\}$  and  $\alpha = \{-2.03^{+0.76}_{-0.07}, -2.36^{+0.17}_{-\infty}, -2.86^{+0.76}_{-\infty}\}$  for the redshift ranges  $2.9 \leq z \leq 4$ ,  $4 < z \leq 5$ , and  $5 < z \leq 6.64$ , respectively. We remark that in Drake et al. (2017a) the 1D confidence intervals on  $L^*$  and  $\alpha$  were estimated by taking the extremes of the  $\Delta S = 1$  contour, i.e. without doing the marginalisation. This estimation implicitly assumes a 2D Gaussian distribution for the likelihoods (James 2006). Nevertheless, we verified that the extremes of the  $\Delta S = 1$  contour are in good agreement with the marginalised confidence limits. But we caution that such 1D errors do, by construction, not reflect the interdependence between  $\alpha$  and  $L^*$ . Importantly, this interdependence needs to be taken into account when discussing the LAE LF redshift evolution based on parametric LF fits. To facilitate such a discussion in future work, we release our obtained  $S(\log L_{\text{Ly}\alpha}, \alpha)$  and  $\phi^*(\log L_{\text{Ly}\alpha}, \alpha)$  functions shown in Figure 12 in machine readable form with this publication.

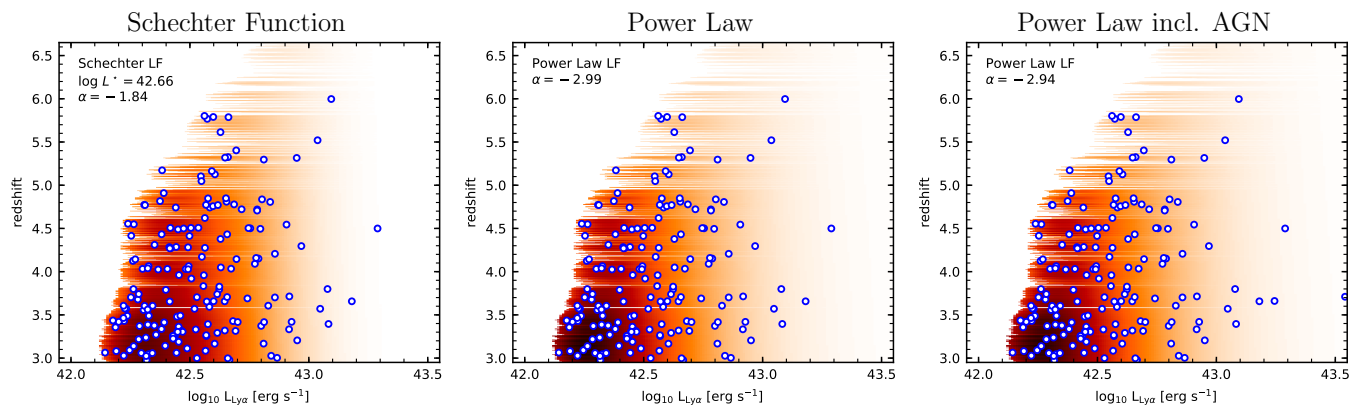


**Fig. 14.** The expected LAE distribution in redshift-luminosity space from the best-fit parameterisations folded with the MW survey area, selection function and  $f_c = 0.15$  truncation criterion is shown in shaded orange (*left*: Schechter Function; *centre*: power law; *right*: power law without excluding the AGN LAEs). The distributions are used to generate random samples to calibrate the 1D and 2D Kolmogorov-Smirnov and Kuiper test statistics. Blue circles show the actual LAE samples in redshift-luminosity space. The 2D KS-test statistic is computed by comparing the actual samples to the model distributions.

**Table 3.**  $p$ -values from Monte-Carlo calibrated KS and Kuiper tests of the observed distribution against maximum-likelihood LF models obtained by folding the maximum-likelihood Schechter (Eq. (19)) or power-law (Eq. (23)) parameterisations with the MW survey area and LAE selection function (RSSF), as well as the  $f_c = 0.15$  truncation criterion. 1D KS and Kuiper tests are performed in redshift and luminosities (see Figures 15, 16 and 17), while the 2D KS test operates directly in redshift-luminosity space (see Figure 14).

Parametrisation	$P_{\text{KS}}^{L_{\text{Ly}\alpha}}$	$P_{\text{Kuiper}}^{L_{\text{Ly}\alpha}}$	$P_{\text{KS}}^z$	$P_{\text{Kuiper}}^z$	$P_{2\text{DKS}}$
Schechter ( $\log L^* = 42.66$ , $\alpha = -1.84$ , $\log \phi^* = -2.71$ )	0.74	0.73	0.30	0.49	0.87
Power Law ( $\log L^* = 42.5$ , $\beta = -2.99$ , $\log \phi^* = -2.932$ )	0.08	0.04	0.17	0.35	0.23
Power Law incl. AGN ( $\log L^* = 42.5$ , $\beta = -2.94$ , $\log \phi^* = -2.930$ )	0.12	0.08	0.18	0.29	0.30

**Notes.**  $L^*$  in  $\text{erg s}^{-1}$  and  $\phi^*$  in  $\text{Mpc}^{-3}$ .

In Figure 13 we compare the maximum-likelihood estimated Schechter function LF to the non-parametric  $1/V_{\text{max}}$ -estimate. The in this figure shown 68.3% and 95.5% confidence limits on the cumulative Schechter function were obtained by randomly drawing<sup>12</sup> 1000 LAE LFs from the normalised likelihood function (Eq. 20). We deliberately compare here the parametric results to the non-parametric  $1/V_{\text{max}}$  estimate, because in both approaches the selection function needs to be integrated over the whole redshift range (compare denominators in Eq. 21 and Eq. 7), which is not the case for the  $C^-$ -method. Thus, a comparison of the maximum-likelihood results to the  $C^-$  results would stand on unequal footing. As evident from Figure 13, there is excellent agreement between the non-parametric and parametric LFs, indicating that indeed the Schechter parameterisation appears qualitatively to be a valid description of the LAE LF.

We also test whether a power-law (Eq. 23) is a more suitable parameterisation of the LAE LF from our MW data. To this aim, we first calculate the inverted log-likelihood function for a fine sampled grid of power-law slopes  $\beta$ . We find the minimum in  $S$  at  $\beta = -2.99 \pm 0.12$ . The normalisation, evaluated at  $\log L^* = 42.5$ , is  $\log \phi^* = -2.932 \pm 0.006$ . We also perform the same analysis without excluding the AGN from the sample. In this case we recover a slope  $\beta = -2.94 \pm 0.12$ , and normalisation  $\log \phi^* = -2.930 \pm 0.006$  (at  $\log L^* = 42.5$ ).

Equipped with these results, we now quantify the goodness-of-fit. Our statistical analysis will enable us to decide whether

the power-law or Schechter parameterisation describes the LAE LF more adequately. A possible statistical test in this respect is the Kuiper test (e.g., Press et al. 1992; Ivezić et al. 2014). This test bears similarities to the well-established Kolmogorov-Smirnov (KS) test, but it is more sensitive to the discrepancies in the wings of the distribution (see also Wisotzki 1998). Hence, it is more suitable for the situation at hand, as the exponential cut-off in the power-law in the Schechter function modulates the expected frequency of the brighter galaxies in our probed luminosity range. Nevertheless, for comparison purposes we also compute the classical KS tests. Both tests are one-dimensional, thus require marginalisation over our sample and the model distributions (explained below), either over redshifts or luminosities. When marginalising over redshifts we thus test for discrepancies between the observed and model luminosity distributions. Given the assumption of a non-evolving LF over the probed redshifts, which was already backed with evidence in the previous section, this marginalisation provides the most powerful metric for testing the different LF parameterisations. Marginalising over luminosities, on the other hand, tests whether the observed distributions in redshifts are adequately described by one parameterisation. This provides us with a parametric test for redshift evolution. Finally, dealing with a 2D distribution in redshift-luminosity space we also calculate a 2D variant of the KS statistic that was originally developed by Peacock (1983).

A possible pitfall when utilising these tests is that we determined the model parameters from the same dataset. As explained in Wisotzki (1998) then the distribution functions of those test

<sup>12</sup> Random draws were realised with the rejection method (Press et al. 1992).

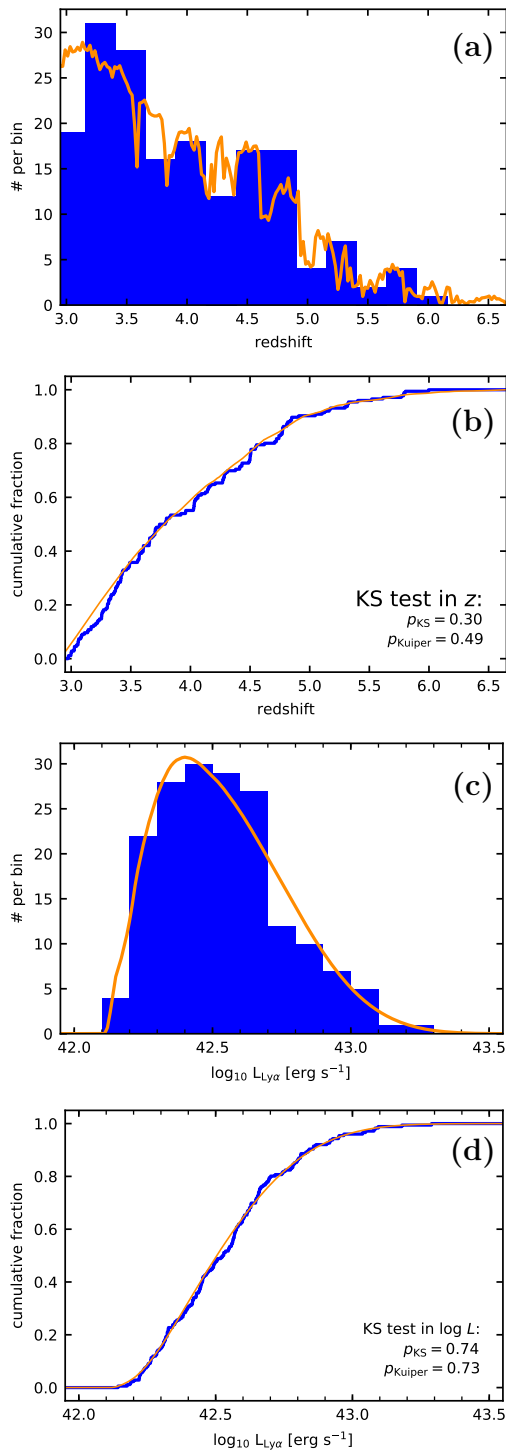


**Fig. 15.** Visualisation of the procedure to calculate the Kuiper- and KS-test statistics. *Panel (a)*: Predicted number counts as a function of redshift from the maximum likelihood Schechter model folded with the MW survey area, selection function (RSSF), and the  $f_c = 0.15$  truncation criterion (orange curve) in comparison to a histogram of the observed number counts (blue histogram). *Panel (b)*: Normalised cumulative distribution in redshift for the Schechter model in panel (a) compared to the observed cumulative distribution. *Panel (c)*: Similar to panel (a), but as a function of Ly $\alpha$  luminosity. *Panel (d)*: Similar to panel (b), but as a function of Ly $\alpha$  luminosity. The Monte-Carlo calibrated  $p$ -values of the KS and Kuiper test are given in panel (b) and (d) – see also Table 3.

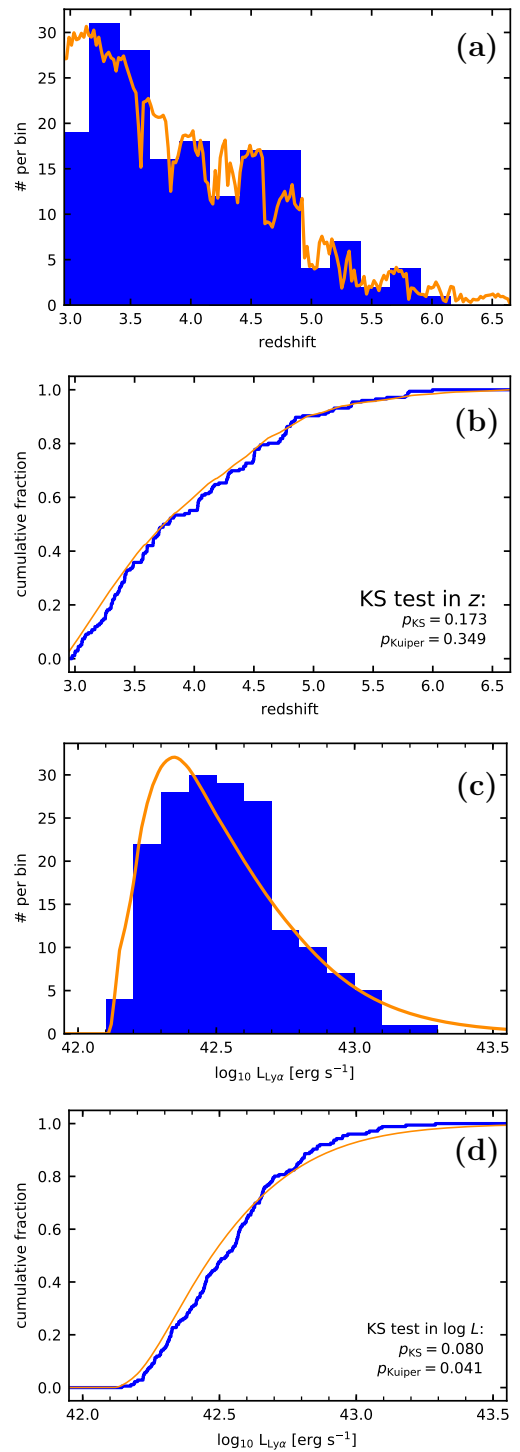


**Fig. 16.** Same as Figure 15, but for the maximum likelihood power law model.

statistics are not valid anymore for calculating  $p$ -values needed to reject or accept the null-hypothesis “data is represented by the model”. This is because the null-hypothesised model has been moved closer to the data due to its estimation from the data. We circumvent this by performing Monte-Carlo simulations to calculate the distribution of these test-statistics under the null-hypothesis (Press et al. 1992, Chapt. 14.3). Therefore we draw a large number of samples of the same size as our LAE

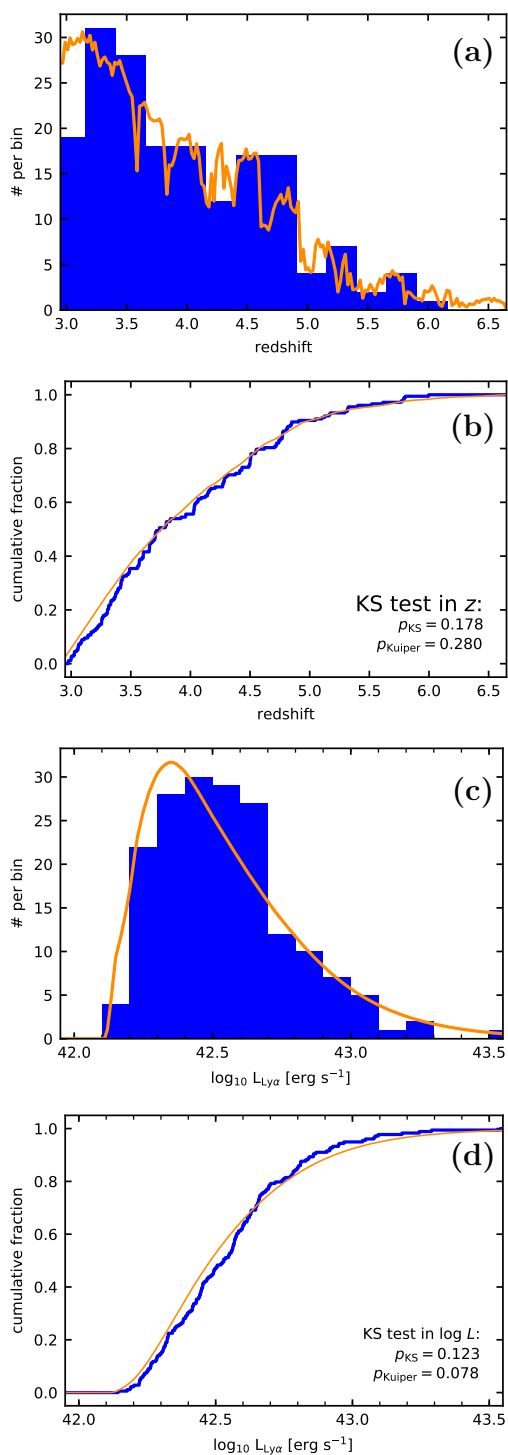


**Fig. 17.** Same as Figure 16, but here the analysis was performed without excluding the AGN from the sample.

LF sample from the ML luminosity function models. In these simulations we account for the surveyed area, the MW selection function (RSSF), and the  $f_c = 0.15$  sample truncation criterion. We show in Figure 14 the resulting 2D distributions in redshift-luminosity space from the maximum-likelihood models together with the MW LAE sample. Moreover, the marginalised differential and cumulative distributions in redshift- or luminosity-space, together with binned histograms of the actual samples are shown

in Figure 15 for the Schechter function, in Figure 16 for the power law, and in Figure 17 for the power law without exclusion of the two AGN in the sample. The 2D KS test-statistics are computed by comparing the 2D model distributions to the actual samples (i.e. from the data shown in Figure 14), and the 1D KS- and Kuiper-tests are computed by comparing the cumulative 1D model distributions to the cumulative sample distribution (i.e. from the data shown in panels (b) and (d) in Figures 15, 16, and 17). We list in Table 3 the resulting  $p$ -values from those tests.

It is visually already apparent, especially when contrasting the panels comparing the cumulative distributions in  $L_{Ly\alpha}$  in Figures 15, 16, and 17 that the expected distributions from the power-law parameterisations show marked discrepancies with respect to the observed distribution. This visual impression is confirmed by the  $p$ -values (Table 3). All three statistical tests result in markedly smaller  $p$ 's for the power law model compared to the  $p$ 's for the Schechter model. The KS- and Kuiper-tests in redshift space result in  $p$ -values at which neither the power-law nor Schechter model can be formally rejected. This shows that a single parameterisation of the LAE LF is adequate to describe the LAE LF over the redshift- and luminosity range probed by MW, but the Schechter model can be favoured due to its markedly higher  $p$ -values. This result is consistent with the non-parametric test presented in the previous section that indicated a non-evolving LAE LF over the redshift range probed by MW (Table 1). Given the non-evolving LF, the resulting  $p = 0.04$  of the Kuiper test in  $L_{Ly\alpha}$  for the power law model means that we can reject this parameterisation at  $2\sigma$  significance. Only when not excluding the X-Ray identified AGN from the LAE sample, the power-law becomes a marginally consistent description of the sample. Based on these results we adopt our ML Schechter model as the working hypothesis for the remainder of this paper.

We noticed that parametric models for LAE LFs in the literature are sometimes obtained by  $\chi^2$ -fitting a model to non-parametric binned estimates of the differential LF (e.g. van Breukelen et al. 2005; Cassata et al. 2011; Matthee et al. 2015; Santos et al. 2016; Sobral et al. 2018b). However, we caution that such an approach does result in model parameters that are not independent on the placement of the bins and the adopted bin width. We visualise this in Figure 18 for our sample. There we show the resulting  $(L^*, \alpha)$  values from a non-linear fit (obtained with the Levenberg-Marquardt algorithm) of the Schechter function (Eq. 19) to different binned  $1/V_{\max}$  estimates (Eq. 8). For this exercise we varied both the size (different panels in Figure 18) and the placement (different colours in Figure 18) of the bins. Moreover, we ignored incomplete bins, i.e. bins with objects that fall below the  $f_c = 0.15$  truncation criterion, in the fitting procedure. As evident, the resulting  $(L^*, \alpha)$  pairs scatter substantially, with only a few combinations of bin-width and bin-placement reproducing the actual ML solution. Thus, such a fitting approach will not lead to a robust parameterisation of the LF. However, given a ML solution it could potentially be used to determine an optimal bin-width and bin-placement at which the binned estimate will be closest to the adopted parametric form. Indeed, for our adopted bin-width ( $\Delta \log L_{Ly\alpha} [\text{erg s}^{-1}] = 0.2$ ) and bin-placement (lowest luminosity boundary  $\log L_{Ly\alpha} [\text{erg s}^{-1}] = 42.2$ ), the parametric fit to the binned data is in very good agreement with the ML solution.

We plot in Figure 19 the non-parametric differential MW LAE LF in three redshift bins ( $2.9 < z \leq 4$ ,  $4 < z \leq 5$ , and  $5 < z \leq 6.7$ ), as well as the global ( $2.9 < z < 6.7$ ) LAE LF. The non-parametric results shown in this figure are obtained with the  $\phi_{\text{PC}}$ -method for the RSSF and the PSSF. For both the redshift bins and the whole redshift range we also display the

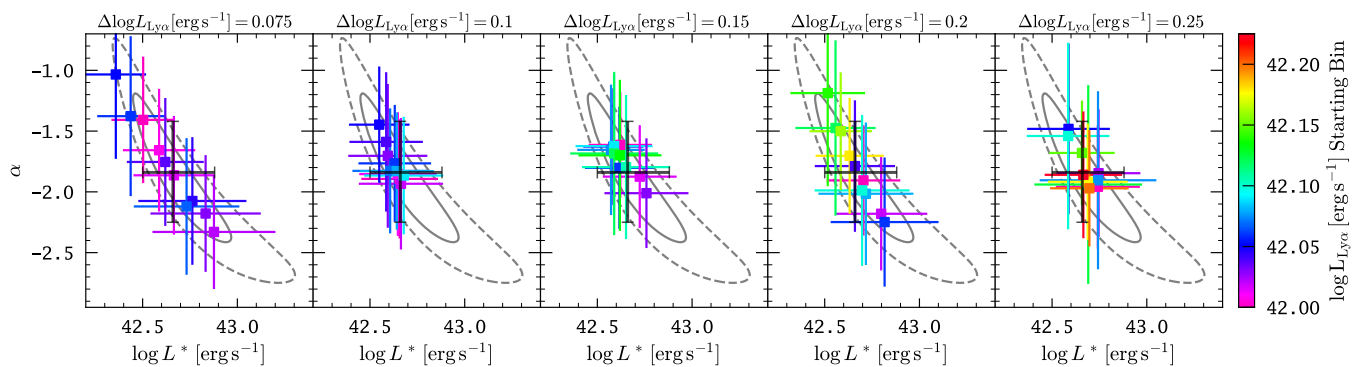


**Fig. 18.** Resulting Schechter parameters  $L^*$  and  $\alpha$  from a non-linear least-squares fit (using the Levenberg-Marquardt algorithm) of the Schechter function (Eq. 19) to the binned differential  $1/V_{\max}$  estimator (Eq. 8) for different binning schemes. Panels from left to right show five different bin-sizes  $\Delta \log L_{\text{Ly}\alpha} [\text{erg s}^{-1}] = \{0.075, 0.1, 0.15, 0.2, 0.25\}$ . Colour coded in each panel is the best-fit  $(L^*, \alpha)$  pair according to the lowest-luminosity boundary of the starting bin. Incomplete bins (containing objects at  $f_c < 0.15$ ) are ignored in the fit, i.e. the magenta point in the panel  $\Delta \log L_{\text{Ly}\alpha} [\text{erg s}^{-1}] = 0.2$  panel represents the adopted binning scheme (cf. Sect. 4.2) in Table 2 and Figure 20. For guidance the likelihood contours and the maximum-likelihood solution from Figure 12 are shown in each panel.

68.3% and 95.4% confidence intervals of the global Schechter LF. As for Figure 13, these intervals were obtained by randomly drawing 1000 LAE LFs from the normalised likelihood function. Here it can be seen that the global Schechter fit is an excellent description of the global binned RSSF LF. This result confirms what we saw already when comparing the parametric to the non-parametric cumulative LAE LFs in Figure 13. Moreover, the binned estimates in the different redshift bins are also in excellent agreement with the global Schechter parameterisation, thus adding further evidence to our previous tests that indicated a non-evolving apparent LAE LF. All these results justify the use of a global LAE LF in this redshift range by MW. Hence, the estimates in the redshift bins here serve only demonstrative purposes and will not be considered further. For the same reason, parametric estimates in the redshift bins are prohibitive for our sample, as they just would lead to a larger uncertainty on the final fitting parameters (so called “overfitting”). We commented already on the upwards correction of the LAE LF by up to a factor of 2.5 at the faint-end of our probed luminosity range when utilising the RSSF instead of the PSSF (Sect. 5.1). Finally, in the here presented comparison between RSSF and PSSF corrected LFs it can be visually appreciated that neglecting extended Ly $\alpha$  emission in the selection function naturally leads to the inference of a flatter faint-end slope  $\alpha$  in the Schechter parameterisation. We will demonstrate in the next section that the PSSF corrected values are in better agreement with previously determined literature estimates.

We also compare in Figure 19 the MW LAE LF to published LAE LF estimates other from MUSE surveys performed within the MUSE consortium (Bina et al. 2016; Drake et al. 2017b,a). Key parameters from those surveys are also listed in Table 4. Both, the binned estimates from the pilot study by Bina et al. (2016), which makes use of the lensing cluster Abell 1689, as well as the global LAE LF determination from the deep MUSE commissioning data in the *Hubble* Deep Field South show some agreement at the  $1\sigma$  level with our estimates. However, the error bars from these early analyses of MUSE data are quite large, and the estimates scatter substantially. More relevant is the good agreement between our results and the binned estimates from the MUSE-Deep programme in the *Hubble* Ultra Deep Field by Drake et al. (2017a). Where the luminosity ranges between MUSE-Deep and the here presented MW sample overlap, the datapoints are in almost perfect agreement, except for

the brightest Drake et al. (2017a) bins for the redshift range  $2.9 < z \leq 4$  and for the global LF. However, the mismatch in those brightest bins is a consequence of the pencil-beam nature of the MUSE Deep survey, making it prone to cosmic variance for such brighter and rarer LAEs. We stress again that the Drake et al. (2017a) study also incorporates a correction for extended Ly $\alpha$  halos in their completeness function estimates. In this respect it is especially encouraging that even their faintest bins ( $\log L_{\text{Ly}\alpha} [\text{erg s}^{-1}] < 42.0$ ) are in agreement with the  $2\sigma$  contours of our extrapolated Schechter parameterisation below the luminosity limit of MW<sup>13</sup>, except at  $z > 5$ . There, however, the faintest bins are below the adopted  $f_c = 0.25$  completeness cutoff for the parametric modelling in Drake et al. (2017a), as at those low completeness levels the selection function was deemed unreliable. The comparison with the MUSE-deep analyses demonstrates how MW is complementary at brighter luminosities. In a forthcoming study we will perform a joint and homogenised LAE LF analysis of the deep and wide MUSE datasets.

## 6. Comparison with the Literature

We now compare the obtained MW LAE LF with previous literature estimates in the redshift range  $3 \lesssim z \lesssim 6$ . For this purpose we utilise the literature compilation of binned differential LAE LF estimates provided by Sobral et al. (2018b), with the exceptions of a few references which were not present in that compilation (namely the studies by Shimasaku et al. 2006, Shioya et al. 2009, Henry et al. 2012<sup>14</sup> and Konno et al. 2018). An overview of the comparison studies is provided in Table 4, where we list their methodology, redshift ranges, survey areas, probed comoving volumes, as well as the lowest Ly $\alpha$  luminosities to which the LAE LF was probed. For the imaging campaigns we also list the adopted equivalent width cuts, as well as the number of photometric LAE candidates and actual spectroscopic confirmations.

Except for the MUSE studies mentioned at the end of the previous section only Sobral et al. (2018b) attempted to construct a global LAE LF over a similar redshift range. We provide a comparison between their binned estimates and our binned and para-

<sup>13</sup> As discussed by Drake et al. (2017a), their faintest bins at  $3 < z < 4$  are consistent with the LAE LF construction at  $z \sim 3$  from a blind 92h long-slit integration with FORS2 by Rauch et al. (2008).

<sup>14</sup> We use the “inferred LAEs, high” LF estimate from Henry et al. (2012), for which also the less certain LAEs were kept in the sample.

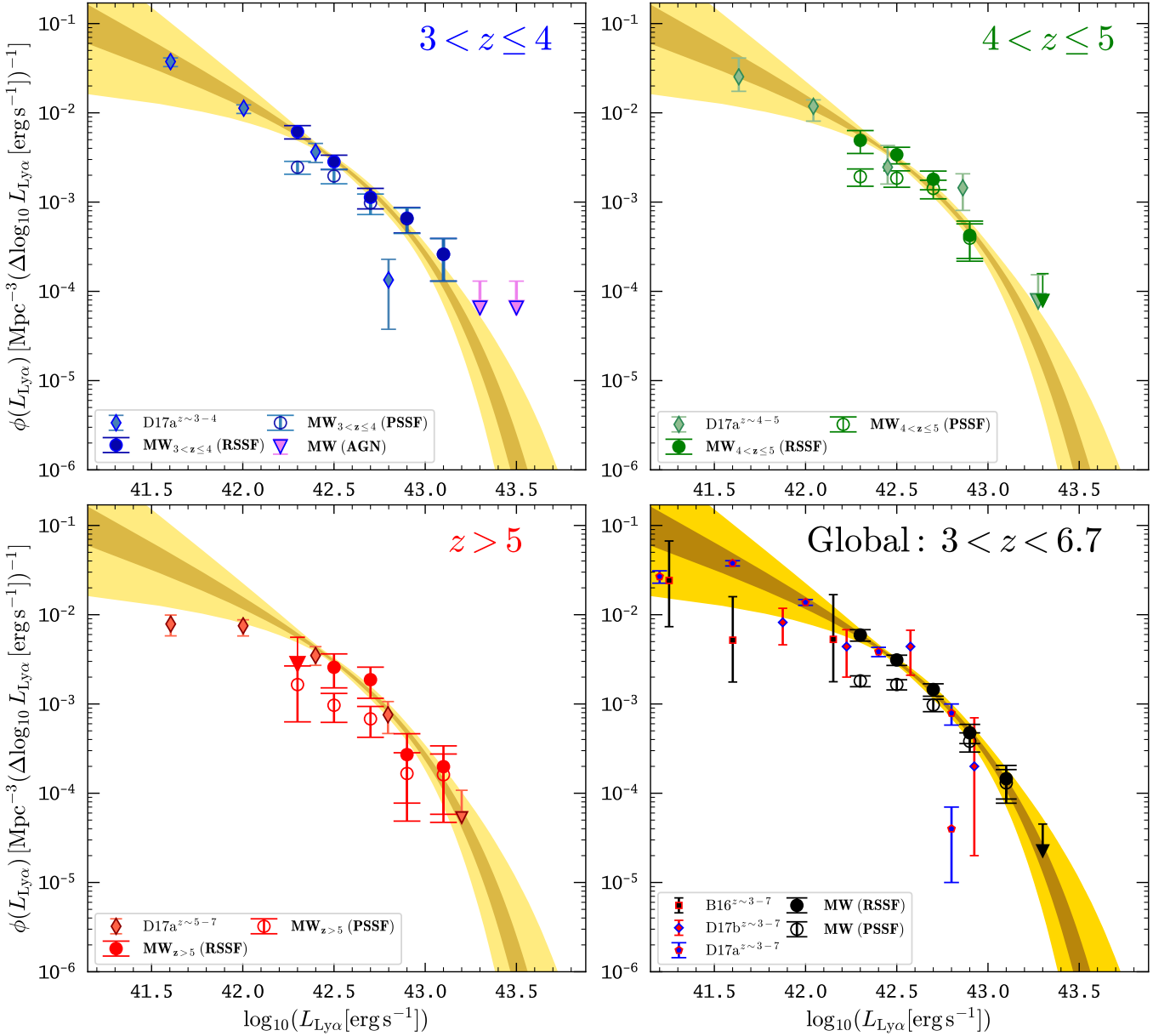


**Fig. 19.** Differential MUSE-Wide LAE LF in the redshift ranges  $2.9 < z \leq 4$  (top left panel),  $4 < z \leq 5$  (top right panel),  $5 < z < 6.7$  (bottom left panel), and for the global MW redshift range (bottom right panel). Our “realistic source selection function” (RSSF, see Sect. 3.2) corrected binned estimates are shown as filled circles, while the with the oversimplified “point source selection function” (PSSF, see Sect. 3.1) corrected binned estimates are shown with open circles. Yellow (dark yellow) shaded regions indicate the 68.3% (95.4%) confidence regions for a Schechter parameterisation obtained a maximum likelihood analysis (Sect. 4.3). For this parametric modelling we corrected with the RSSF for completeness. Also shown in this figure are other MUSE LAE estimates obtained by the MUSE GTO consortium, namely the binned estimates by Drake et al. (2017b) obtained from MUSE commissioning observations in the *Hubble* Deep Field South, the binned estimates by Drake et al. (2017a) from the MUSE-Deep observations in the *Hubble* Ultra Deep Field, and the pilot study by Bina et al. (2016) exploiting gravitational lensing by the lensing cluster Abell 1689.

metric estimates in Figure 20. Where the MW luminosity range overlaps with SC4K, both LF estimates are in agreement, except for the faintest SC4K bins. These bins fall below our RSSF corrected results and line up closer with our PSSF corrected estimates. We will comment on this mismatch at the faint end below, as it seems to be a generic property of previous LAE LF construction attempts.

First we focus in Figure 20 on the bright end of the global SC4K LAE LF ( $\log L_{Ly\alpha} \gtrsim 43.2$ ). There we note an apparent excess of the Sobral et al. (2018b) bins compared our the  $1\sigma$  contours of our extrapolated Schechter parameterisation. In fact,

the display of our binned RSSF-corrected estimate together with the SC4K binned estimate is very suggestive of a non-existent “knee” in the LAE LF and thus indeed supportive of the power-law parameterisation favoured by Sobral et al. (2018b). This is not in tension with our statistical analysis presented in Sect. 5.2 that disfavoured a power-law. The reason could simply be the limited dynamical range in high  $Ly\alpha$  luminosities. Such bright and rare LAEs are only sampled with robust statistics in wide-field NB imaging campaigns. Notably, also several other studies also indicate that a non-exponential drop-off at the bright-end of the LAE LF is not required, both at lower redshifts ( $z \lesssim 2$ , Konno

**Table 4.** Compilation of key parameters of LAE LF studies from the literature in the redshift range probed by MW.

Reference	Method <sup>(*)</sup>	$EW_{Ly\alpha}^{lim}$ [Å]	$z$	Area [deg <sup>2</sup> ]	Volume [Mpc <sup>3</sup> ]	$\log L_{Ly\alpha,lim}$ log [erg s <sup>-1</sup> ]	$N_{phot}^{(**)}$	$N_{spec}^{(**)}$
Ouchi et al. (2008)	SC/NB503	64	$3.1 \pm 0.03$	0.983	$7 \times 10^5$	42.0	356	41
...	SC/NB570	44	$3.7 \pm 0.03$	0.965	$6.1 \times 10^5$	42.6	101	26
...	SC/NB816	27	$5.7 \pm 0.05$	1.033	$9.2 \times 10^5$	42.5	401	17
Grove et al. (2009)	FORS2/3NB	25	2.85/3.15/3.25	0.037	$1.4 \times 10^4$	41.5	83	59
Cassata et al. (2011)	VIMOS	-	2 – 6.6	0.62/0.16 <sup>†</sup>	-	41.0	84 <sup>††</sup>	153 <sup>††</sup>
Matthee et al. (2017)	INT/NB501	12	$3.06 \leq z \leq 3.17$	0.7	$7.2 \times 10^5$	43.0	32	5
Sobral et al. (2018b)	SC/IA464-527 <sup>#</sup>	50	$3.1 \pm 0.4$	$\approx 2$	$17.3 \times 10^6$	42.5	2146	? <sup>‡</sup>
...	SC/IA574,624	50	$3.9 \pm 0.3$	$\approx 2$	$10.1 \times 10^6$	42.95	240	? <sup>‡</sup>
...	SC/IA679,709	50	$4.7 \pm 0.2$	$\approx 2$	$10.6 \times 10^6$	43.1	160	? <sup>‡</sup>
...	SC/IA738-827 <sup>‡</sup>	50	$5.4 \pm 0.5$	$\approx 2$	$15.5 \times 10^6$	43.3	147	? <sup>‡</sup>
...	SC4K/global	50	$\sim 2.5 - 6$	$\approx 2$	$\sim 10^8$	42.5	3434	112 <sup>‡</sup>
Drake et al. (2017a)	MUSE/HUDF	-	$3.5 \pm 0.5$	$7 \times 10^{-7}$	$3.1 \times 10^4$	41.0	-	193
...	...	-	$4.5 \pm 0.5$	$7 \times 10^{-7}$	$2.6 \times 10^4$	41.0	-	144
...	...	-	$5.8 \pm 0.8$	$7 \times 10^{-7}$	$3.6 \times 10^4$	41.0	-	50
...	...	-	2.91 – 6.64	$7 \times 10^{-7}$	$9.3 \times 10^4$	41.0	-	387
Drake et al. (2017b)	MUSE/HDFS	-	2.91 – 6.64	$8 \times 10^{-8}$	$1 \times 10^4$	41.4	-	59
Dawson et al. (2007)	4m/5NB	15	$4.4 \pm 0.1$	$2 \times 10^{-4}$	$1.5 \times 10^4$	42.0	97	79
Shioya et al. (2009)	SC/NB711	12	$4.86 \pm 0.03$	1.83	$1.1 \times 10^6$	42.8	79	0
Konno et al. (2018)	HSC/NB816	10	$5.73 \pm 0.05$	13.8	$1.2 \times 10^7$	42.9	1077	49
Shimasaku et al. (2006)	SC/NB816	10	$5.7 \pm 0.05$	0.2	$1.8 \times 10^5$	42.5	89	39
Santos et al. (2016)	SC/NB816	25	$5.7 \pm 0.05$	7	$6 \times 10^6$	42.4	514	46
Henry et al. (2012)	IMACS/NB+slits	-	$5.7 \pm 0.1$	0.015	$1.5 \times 10^4$	42.1	105 <sup>‡‡</sup>	6
Bina et al. (2016)	MUSE/Abell1689	-	2.91 – 6.64	$8 \times 10^{-8}$	900 <sup>b</sup>	40.5	-	17

**Notes.**

(<sup>\*</sup>): Legend for abbreviations: SC/X=Subaru Suprime-Cam with filter X; HSC/NB816=Subaru Hyper Suprime-Cam with NB816 filter; FORS2/3NB=ESO VLT/FORS2 - 3 fields, with 3 different narrow-band filters; VIMOS=ESO VLT/VIMOS multi-slit spectroscopic survey; INT/NB501= Wide-Field Camera with NB501 filter at Isaac Newton 2.5m Telescope; MUSE/HUDF=MUSE Hubble Ultra Deep Field; MUSE/HDFS=MUSE Hubble Deep Field South; 4m/5NB=5 overlapping narrow-band filters on two 4m class telescopes; IMACS/NB+slits=Multi-slit narrow-band spectroscopic search with IMACS on the Baade telescope (see also Martin et al. 2008); MUSE/Abell1689=MUSE observations of the lensing cluster Abell 1689.

(<sup>\*\*</sup>): Number of photometrically selected LAE candidates ( $N_{phot}$ ) and number of spectroscopic confirmations ( $N_{spec}$ ).

<sup>†</sup>: Area of the imaging campaign (VIMOS Deep Survey / VIMOS Ultra Deep Survey) from which targets were pre-selected for VIMOS multi-slit spectroscopy.

<sup>††</sup>: Here  $N_{phot}$  refers to the number of photometrically pre-selected LAEs, while  $N_{spec}$  indicates the number of serendipitously detected sources.

<sup>‡</sup>: Spectroscopic confirmations only reported for the combined SC4K sample.

<sup>‡‡</sup>: Single unresolved emission line objects without continuum detections (see also Martin et al. 2008).

<sup>#</sup>: IA464, IA484, IA505, and IA527 medium band filters.

<sup>‡</sup>: IA738, IA767, and IA827 medium band filters.

<sup>b</sup>: Effective comoving volume from lensing magnification.

et al. 2016; Wold et al. 2017; Hao et al. 2018) and at higher redshifts ( $z \gtrsim 5$ , Santos et al. 2016; Matthee et al. 2017; Bagley et al. 2017). While the low redshift studies demonstrate convincingly that the excess at the bright end of the LAE LF can almost exclusively be attributed to AGN (see especially Konno et al. 2016; Wold et al. 2017), the nature of these sources at high-redshifts appears to be less clear. Another hint at the possible mismatch of our favoured Schechter model with the bright end of the LAE LF can also be seen in Figure 21, where we compare the  $1\sigma$  and  $2\sigma$  contours of the global Schechter parameterisation from our likelihood analysis with binned estimates from the literature in different redshift ranges. However, there is considerable scatter amongst the literature estimates, even amongst the different red-

shift slices from the SC4K survey, and at least most of the data points are consistent at the  $2\sigma$  level with the Schechter model.

If the bright-end excess seen in the LAE LF can not be attributed to AGN activity (e.g. Sobral et al. 2018b excluded AGN based on X-Ray and radio diagnostics), then the LAE LF would be of different shape compared to the rest-frame ultra-violet (UV) LF of high-redshift galaxies which appears to be well described by a Schechter function (e.g. Bouwens et al. 2007, 2015). However, the most recent wide area ground based surveys start to question this result by reporting a bright-end excess in the UV LF that can not be solely attributed to AGN activity and seems to deviate from a simple Schechter parameterisation (Ono et al. 2018; Viironen et al. 2018). Certainly, Ly $\alpha$  radi-

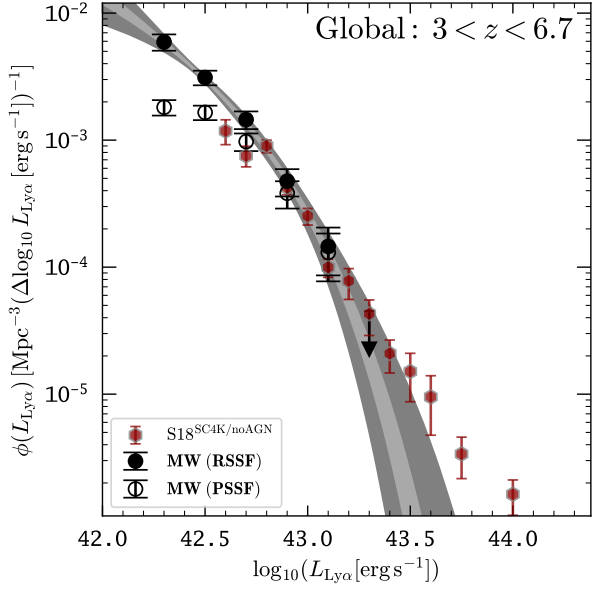


**Fig. 20.** Global ( $2.9 \leq z \leq 6$ ) MUSE-Wide LAE LF (binned RSSF and PSSF corrected results from filled and open circles, respectively) with  $1\sigma$  (dark grey shaded region) and  $2\sigma$  intervals (grey shaded region) for the RSSF corrected Schechter parameterisation as in the bottom right panel of Figure 19, in comparison to the binned estimates of the global ( $2.5 \leq z \leq 6$ ) SC4K LAE LF (Sobral et al. 2018b).

tive transfer is expected to modulate the Ly $\alpha$  output of a galaxy compared to its overall ionising photon production, which as a good first-order approximation can be traced by its UV luminosity (e.g. Bouwens et al. 2016; Schaerer et al. 2016). In principle the UV and LAE LFs can be linked to each other (Henry et al. 2012; Gronke et al. 2015). However, in which way radiative transfer processes or additional Ly $\alpha$  photon production processes (e.g., ionising photons from UV undetected satellite galaxies or Ly $\alpha$  boosting from the UV background as proposed in Mas-Ribas & Dijkstra 2016) could influence the bright-end of the LAE LF compared to the bright end of the UV LF remains currently purely speculative. Indeed, a few of the most-luminous LAES at  $z \gtrsim 6$  have already received observational attention (e.g. Ouchi et al. 2009; Lidman et al. 2012; Hu et al. 2016; Matthee et al. 2018), with one object being suggested to either host metal-free stars (Sobral et al. 2015) or a direct-collapse black hole (Pallottini et al. 2015). At  $z \sim 2 - 3$  Sobral et al. (2018a) presented recently spectroscopic results on 20 bright LAEs ( $\log L_{\text{Ly}\alpha} [\text{erg s}^{-1}] > 42.7$ ). Interestingly, these authors report a 60% AGN fraction for such luminous LAEs, which rises sharply to 100% for  $\log L_{\text{Ly}\alpha} [\text{erg s}^{-1}] > 43.3$ . This indeed suggests that the observed deviations from a Schechter function at bright luminosities are caused by sources whose Ly $\alpha$  emission is powered by non-thermal black hole accretion processes, rather than star formation.

We also find some notable overall disagreements between the literature and our estimates in luminosity range where MW overlaps with other surveys. In the redshift range  $2.9 < z \leq 4$  (top-left panel in Figure 21) we find that our LF is significantly higher (i.e. up to an order of magnitude) compared to the LF estimates obtained by Cassata et al. (2011). But, the Cassata et al.  $z \sim 3 - 4$  LF is also significantly below most other literature estimates and it is only consistent with the faint end ( $\log L_{\text{Ly}\alpha} [\text{erg s}^{-1}] \leq 42.5$ ) of the Grove et al. (2009) LF. Moreover, also most of the LF bins

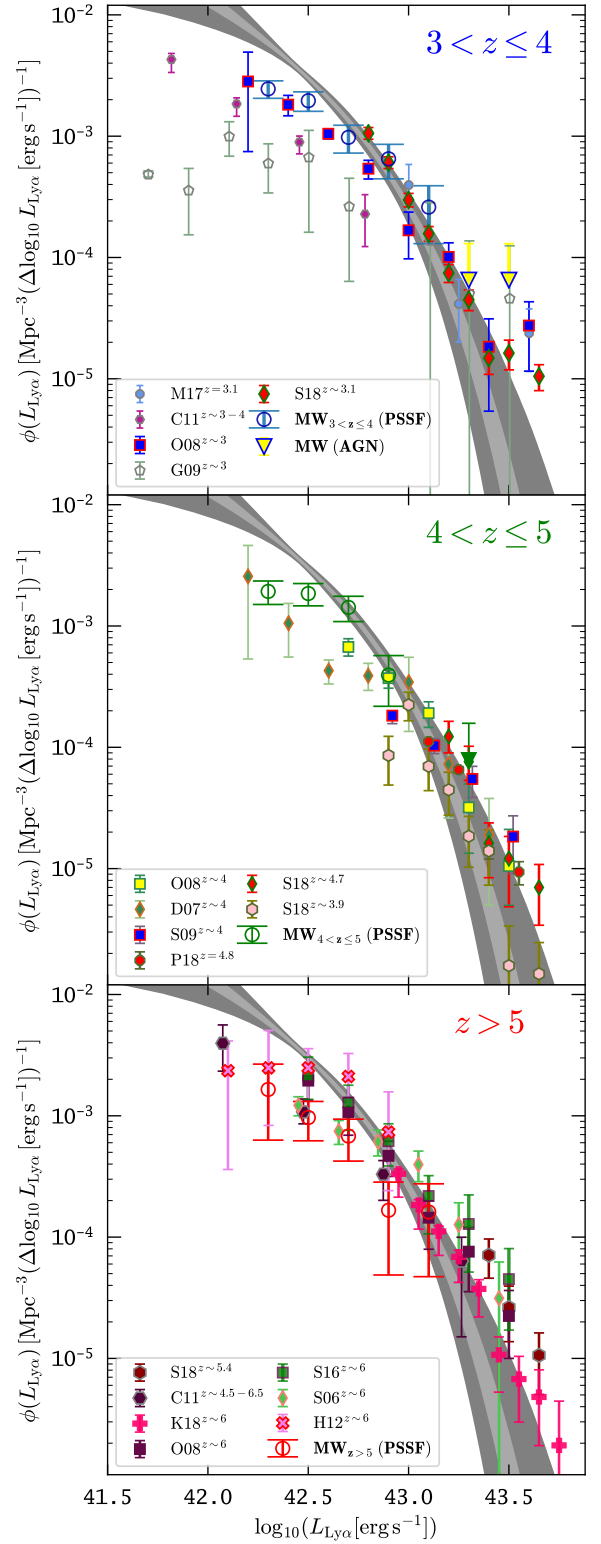


**Fig. 21.** Differential LAE LF estimates from the literature grouped in three redshift bins ( $2.9 < z \leq 4$  in the *top panel*,  $4 < z \leq 5$  in the *middle panel*, and  $5 < z \leq 6$  in the *bottom panel*) compared to our  $1\sigma$  (dark grey shaded region) and  $2\sigma$  intervals (grey shaded region) for the RSSF corrected global Schechter parameterisation (shown already in Figure 19 and Figure 20). References are provided in Table 4, in the legend we abbreviate always with the first letter of the first author and the last two digits of publication year. We also show our PSSF corrected binned estimates as open circles, as those are often in better agreement with the literature estimates (see text).

from Dawson et al. (2007)  $z \sim 4$  (centre panel in Figure 21) are significant below our inferred LF.

Finally, we find from the comparison in Figure 21, where we group the literature results in three redshift bins that the majority of literature LF estimates at luminosities  $\log L_{\text{Ly}\alpha} \lesssim 42.5$  falls below our global Schechter parameterisation. We stress again that this parameterisation was obtained by implicitly correcting for extended low-surface brightness Ly $\alpha$  halos by utilising our RSSF. In this respect it is especially interesting that the majority of the literature estimates are often in nearly perfect agreement with our PSSF completeness corrected LF estimates. Especially the binned estimates of Ouchi et al. (2008) at  $z \sim 3$ , as well as the binned estimate from Shimasaku et al. (2006) and Cassata et al. (2011) at  $z \sim 6$  line up perfectly with our PSSF corrected estimates. Thus, we are able to reproduce the results of previous campaigns by using a completeness correction that is comparable to the ones applied in those studies.

Notably, almost all LAE LF estimates in the literature so far did not take the extended nature of LAEs into account when constructing their selection functions. For example, Ouchi et al. (2008) populate their narrow band imaging data with fake point sources, while Hao et al. (2018), at  $z \sim 2$ , rescale the flux of stellar images in their images. A slightly different approach was used by Konno et al. (2018) utilise a Sèrsic  $n = 1.5$  surface-brightness profile with small effective radii of  $r_e = 0.9$  kpc, but also these fake sources do not correctly represent the typical extended Ly $\alpha$  surface-brightness profiles. As the source detection algorithms used in those surveys utilise parameters optimised for the detection of compact sources, we argue that the inferred selection functions in those studies must be overoptimistic. As we will elaborate later, this leads to a bias in the luminosity function estimate near the completeness limit of the surveys, thus leading to wrong estimates on the faint end of the LAE LF. Moreover, for the faint end studies at  $z \sim 6.5$  appear to be in subtle disagreement (Ouchi et al. 2010; Matthee et al. 2015). Interestingly, Matthee et al. (2015) followed a different approach compared to Ouchi et al. (2010) to estimate their completeness by rescaling fluxes of other sources in the narrow-band filter that do not show an excess but otherwise fulfil the additional colour-selection criteria. Nevertheless, this model-independent approach, utilised also in Sobral et al. (2018b), neglects that a significant fraction of Ly $\alpha$  emission comes from the diffuse low-SB halo.

We argue here that assuming LAEs to be compact “point-like” sources is not a justifiable simplification anymore. As already mentioned in Sect. 5.1, Grove et al. (2009) suspected an inherent bias in LAE LF estimates caused by ignoring possible extended emission in the construction of the selection function. Moreover, the LAEs found in the deep long-slit integration of Rauch et al. (2008), as well as the stacking analyses by Steidel et al. (2011) and Momose et al. (2014) already hinted at a large fraction of LAEs being surrounded by low surface-brightness Ly $\alpha$  halos. Now, from the MUSE deep fields, the omnipresence of Ly $\alpha$  halos around LAEs is a well established fact on an object-by-object basis (Wisotzki et al. 2016; Leclercq et al. 2017). Here we show that accounting for this effect results in an upward correction by a factor of up to three for LF bins at  $\log L_{\text{Ly}\alpha} [\text{erg s}^{-1}] \lesssim 42.5$  of previous surveys.

## 7. Summary and Outlook

We presented a framework for constructing the LAE LF in an integral field spectroscopic survey. We utilised these methods on the LAE sample resulting from the first instalment of the MW survey. Our LAE LF sample covers luminosities  $42.2 \lesssim$

$\log L_{\text{Ly}\alpha} [\text{erg s}^{-1}] \leq 43.5$ . We showed that the apparent LAE LF in this luminosity range is non-evolving over the redshift range  $2.9 \leq z \leq 6.7$ . This result is irrespective of the assumed selection function, but we argued that the classical assumption of LAEs being compact-point like objects biases LF estimates too low near the completeness limit of a survey. We found that different non-parametric estimates provide nearly identical descriptions of the cumulative or differential LAE LF. We obtained a maximum-likelihood Schechter parameterisation of the LAE LF for  $\log L^* [\text{erg s}^{-1}] = 42.66^{+0.22}_{-0.16}$ , and  $\alpha = -1.84^{+0.42}_{-0.42}$ , but with a strong degeneracy between both parameters. The a-posteriori normalisation of the maximum-likelihood Schechter fit is  $\log \phi^* [\text{Mpc}^{-3}] = -2.71$ . We showed that the Schechter parameterisation accurately describes our non-parametric cumulative and differential estimates, while parametrising the LAE LF with a simple power-law provided a less optimal fit. A comparison of our LAE LF with binned estimates of the differential estimates from the literature revealed subtle disagreements. Especially at fainter luminosities ( $\log L_{\text{Ly}\alpha} [\text{erg s}^{-1}] \lesssim 42.5$ ) our LF, and the Drake et al. (2017a) MUSE HUDF LAE LF, are higher than the literature LF estimates. This is a natural consequence of incorporating the dilution of detectable Ly $\alpha$  signal due to extended low-surface brightness Ly $\alpha$  haloes into the completeness correction. We showed that we achieve a better agreement with the literature when assuming for the completeness correction that LAEs are compact point-like sources. However, in light of the recently accumulated evidence regarding the ubiquity of extended Ly $\alpha$  haloes we argued that this is an oversimplified assumption.

With the release of the full MW dataset (Urrutia et al., in prep.) we will significantly improve the statistical robustness of the here presented results due to the by a factor of more than five increased sample size. The main draw-backs of the current data is the lack of a sizeable sample of  $z > 5$  LAEs, and the small number of very luminous ( $\log L_{\text{Ly}\alpha} [\text{erg s}^{-1}] > 43.0$ ) LAEs. Yet, it is especially this currently under-sampled region in the  $(L_{\text{Ly}\alpha}, z)$ -parameter space where other campaigns hint at a possible evolution in the shape and normalisation of the LAE LF (e.g. Santos et al. 2016; Sobral et al. 2018b). While measuring robustly the LF for the most luminous LAEs will remain a domain of the wide-area NB campaigns, MW nicely populates the Ly $\alpha$  luminosity range that overlaps with the faintest ends of such campaigns and the bright ends of the MUSE deep surveys. The next step in our analysis will be the construction of a combined LAE LF from the final MW data set and the MUSE deep fields.

Of course, with an increased sample size on the horizon, we need to be aware of possible systematic uncertainties in the here presented framework. Firstly, all the here applied non-parametric and parametric LF estimators do not take photometric uncertainties into account. Secondly, we do not account for uncertainties in the selection function.

Regarding the selection function construction we assumed that the 10 LAEs from the source insertion and recovery experiment in the HDFS are representative of the whole population, and thus we weighted them equally. We can justify this approach, as no scaling relations between Ly $\alpha$  halo flux fraction and other physical properties have been found. Especially, the halo-flux fraction appears to be independent of Ly $\alpha$  luminosity (Leclercq et al. 2017). And, as we explained in Sect. 3.2, the used sources span a range in halo flux fractions and line profiles. Nevertheless, as of yet we do not have a for selection effects corrected distribution of halo flux fractions. Equipped with such a distribution in the future, a more realistic weighting scheme could be employed.

However, a more relevant systematic effect might result from ignoring the statistical errors on the flux measurement in the LF construction. It is known that especially near the completeness limit of a survey, where also the photometric uncertainties become larger that ignoring photometric errors systematically biases the LF. This bias is referred to as *Eddington-Malmquist*-bias in the literature (see, e.g., Sect. 5.5 in Ivezić et al. 2014). The bias is a combined effect of photometric errors, sample truncation on observed values, and a rising luminosity function towards fainter luminosities. The effect is that near the completeness limit more sources scatter into the sample, than sources which scatter out of the sample. Ultimately this results in higher inferred number source densities at the faint end of the probed luminosity range, and consequentially also to higher inferred slopes in parametric LF determinations. We point out that our sample truncation was quite conservative (Sect. 4.2), i.e. we excluded almost 1/4th of the faintest sources from our final LAE LF sample. Moreover, in the binned estimates the bin-size was chosen to be larger than the photometric error in the faintest bin and the number of sources scattering between the two faintest appears to compensate each other in both directions. A more quantitative discussion is outside the scope of this analysis, but we remark that the *Eddington-Malmquist*-bias has not been commented upon in the LAE LF literature. We argue that robust determinations of the faint end slope need to account for this bias in the future, e.g. by modelling the dependence of the photometric uncertainties on the inferred LFs. Of interest in this respect appears the modified ML estimator developed by Mehta et al. (2015), that can account for photometric uncertainties. Methods like this will allow for a robust and unbiased determination of LAE LFs in the future from which in turn vital key information regarding cosmology and galaxy formation can be extracted.

*Acknowledgements.* We thank the support staff at ESOs VLT for help with the visitor mode observations during GTO. This research made extensive use of the *astropy* package (Astropy Collaboration et al. 2013). All plots in this paper were created using *matplotlib* (Hunter 2007). E.C.H, R.S., T.U., and L.W. acknowledge funding by the Competitive Fund of the Leibniz Association through grants SAW-2013-AIP-4 and SAW-2015-AIP-2. ECH dedicates this paper to Melli's kittens Mary and Jamie.

## References

Adams, J. J., Blanc, G. A., Hill, G. J., et al. 2011, *ApJS*, 192, 5  
 Ajiki, M., Taniguchi, Y., Fujita, S. S., et al. 2004, *PASJ*, 56, 597  
 Astropy Collaboration, Robitaille, T. P., Tollerud, E. J., et al. 2013, *A&A*, 558, A33  
 Bacon, R., Bauer, S.-M., Bower, R., et al. 2004, in Society of Photo-Optical Instrumentation Engineers (SPIE) Conference Series, Vol. 5492, Society of Photo-Optical Instrumentation Engineers (SPIE) Conference Series, ed. A. F. M. Moorwood & M. Iye, 1145–1149  
 Bacon, R., Brinchmann, J., Richard, J., et al. 2015, *A&A*, 575, A75  
 Bacon, R., Conseil, S., Mary, D., et al. 2017, *A&A*, 608, A1  
 Bacon, R. & Monnet, G. J. 2017, *Optical 3D-Spectroscopy for Astronomy* (Wiley-VCH Verlag GmbH & Co. KGaA)  
 Bacon, R., Vernet, J., Borisiva, E., et al. 2014, *The Messenger*, 157, 13  
 Bagley, M. B., Scarlata, C., Henry, A., et al. 2017, *ApJ*, 837, 11  
 Beckwith, S. V. W., Stiavelli, M., Koekemoer, A. M., et al. 2006, *AJ*, 132, 1729  
 Bina, D., Pelló, R., Richard, J., et al. 2016, *A&A*, 590, A14  
 Blanc, G. A., Adams, J. J., Gebhardt, K., et al. 2011, *ApJ*, 736, 31  
 Bouwens, R. J., Illingworth, G. D., Franx, M., & Ford, H. 2007, *ApJ*, 670, 928  
 Bouwens, R. J., Illingworth, G. D., Oesch, P. A., et al. 2015, *ApJ*, 803, 34  
 Bouwens, R. J., Smit, R., Labbé, I., et al. 2016, *ApJ*, 831, 176  
 Caditz, D. M. 2016, *ApJ*, 831, 50  
 Caillier, P., Accardo, M., Adjali, L., et al. 2014, in *Proc. SPIE*, Vol. 9150, Modeling, Systems Engineering, and Project Management for Astronomy VI, 91500D  
 Cassertano, S., de Mello, D., Dickinson, M., et al. 2000, *AJ*, 120, 2747  
 Cassata, P., Le Fèvre, O., Garilli, B., et al. 2011, *A&A*, 525, A143  
 Conseil, S., Bacon, R., Piqueras, L., & Shepherd, M. 2016 [1612.05308]

Cowie, L. L. & Hu, E. M. 1998, *AJ*, 115, 1319  
 Dawson, S., Rhoads, J. E., Malhotra, S., et al. 2007, *ApJ*, 671, 1227  
 Drake, A. B., Garel, T., Wisotzki, L., et al. 2017a, *A&A*, 608, A6  
 Drake, A. B., Guiderdoni, B., Blaizot, J., et al. 2017b, *MNRAS*, 471, 267  
 Dunlop, J. S. 2013, in *Astrophysics and Space Science Library*, Vol. 396, The First Galaxies, ed. T. Wiklind, B. Mobasher, & V. Bromm, 223  
 Efron, B. & Petrosian, V. 1992, *ApJ*, 399, 345  
 Fan, X., Strauss, M. A., Schneider, D. P., et al. 2001, *AJ*, 121, 54  
 Felten, J. E. 1976, *ApJ*, 207, 700  
 Furusawa, H., Kosugi, G., Akiyama, M., et al. 2008, *ApJS*, 176, 1  
 Giavalisco, M., Ferguson, H. C., Koekemoer, A. M., et al. 2004, *ApJ*, 600, L93  
 Grogin, N. A., Kocevski, D. D., Faber, S. M., et al. 2011, *ApJS*, 197, 35  
 Gronke, M., Dijkstra, M., Trenti, M., & Wyithe, S. 2015, *MNRAS*, 449, 1284  
 Gronwall, C., Ciardullo, R., Hickey, T., et al. 2007, *ApJ*, 667, 79  
 Grove, L. F., Fynbo, J. P. U., Ledoux, C., et al. 2009, *A&A*, 497, 689  
 Hao, C.-N., Huang, J.-S., Xia, X., et al. 2018, *ArXiv e-prints* [arXiv:1808.02704]  
 Henry, A. L., Martin, C. L., Dressler, A., Sawicki, M., & McCarthy, P. 2012, *ApJ*, 744, 149  
 Herenz, E. C., Urrutia, T., Wisotzki, L., et al. 2017, *A&A*, 606, A12  
 Herenz, E. C. & Wisotzki, L. 2017, *A&A*, 602, A111  
 Herenz, E. C. & Wisotzki, L. 2016, *LSDCat: Line Source Detection and Cataloguing Tool*, *Astrophysics Source Code Library*  
 Hill, G. J., Gebhardt, K., Komatsu, E., et al. 2008, in *Astronomical Society of the Pacific Conference Series*, Vol. 399, Panoramic Views of Galaxy Formation and Evolution, ed. T. Kodama, T. Yamada, & K. Aoki, 115  
 Hill, G. J. & HETDEX Consortium. 2016, in *Astronomical Society of the Pacific Conference Series*, Vol. 507, Multi-Object Spectroscopy in the Next Decade: Big Questions, Large Surveys, and Wide Fields, ed. I. Skillen, M. Barcells, & S. Trager, 393  
 Hogg, D. W. 1999, *ArXiv Astrophysics e-prints* [astro-ph/9905116]  
 Hu, E. M., Cowie, L. L., Capak, P., et al. 2004, *AJ*, 127, 563  
 Hu, E. M., Cowie, L. L., & McMahon, R. G. 1998, *ApJ*, 502, L99  
 Hu, E. M., Cowie, L. L., Songaila, A., et al. 2016, *ApJ*, 825, L7  
 Hu, E. M. & McMahon, R. G. 1996, *Nature*, 382, 231  
 Hunter, J. D. 2007, *Computing In Science & Engineering*, 9, 90  
 Inami, H., Bacon, R., Brinchmann, J., et al. 2017, *A&A*, 608, A2  
 Ivezić, Ž., Connolly, A. J., VanderPlas, J. T., & Gray, A. 2014, *Statistics, Data Mining, and Machine Learning in Astronomy*  
 James, F. 2006, *Statistical Methods in Experimental Physics: 2nd Edition* (World Scientific Publishing Co)  
 Johnston, R. 2011, *A&A Rev.*, 19, 41  
 Kerutt, J. 2017, *QtClassify: IFS data emission line candidates classifier*, *Astrophysics Source Code Library*  
 Koekemoer, A. M., Faber, S. M., Ferguson, H. C., et al. 2011, *ApJS*, 197, 36  
 Konno, A., Ouchi, M., Nakajima, K., et al. 2016, *ApJ*, 823, 20  
 Konno, A., Ouchi, M., Shibuya, T., et al. 2018, *PASJ*, 70, S16  
 Kron, R. G. 1980, *ApJS*, 43, 305  
 Kudritzki, R.-P., Méndez, R. H., Feldmeier, J. J., et al. 2000, *ApJ*, 536, 19  
 Le Fèvre, O., Saisse, M., Mancini, D., et al. 2003, in *Society of Photo-Optical Instrumentation Engineers (SPIE) Conference Series*, Vol. 4841, Society of Photo-Optical Instrumentation Engineers (SPIE) Conference Series, ed. M. Iye & A. F. M. Moorwood, 1670–1681  
 Leclercq, F., Bacon, R., Wisotzki, L., et al. 2017, *A&A*, 608, A8  
 Lidman, C., Hayes, M., Jones, D. H., et al. 2012, *MNRAS*, 420, 1946  
 Luo, B., Brandt, W. N., Xue, Y. Q., et al. 2017, *ApJS*, 228, 2  
 Lynden-Bell, D. 1971, *MNRAS*, 155, 95  
 Martin, C. L., Sawicki, M., Dressler, A., & McCarthy, P. 2008, *ApJ*, 679, 942  
 Mas-Ribas, L. & Dijkstra, M. 2016, *ApJ*, 822, 84  
 Matthee, J., Sobral, D., Best, P., et al. 2017, *MNRAS*, 471, 629  
 Matthee, J., Sobral, D., Gronke, M., et al. 2018, *ArXiv e-prints* [arXiv:1805.11621]  
 Matthee, J., Sobral, D., Santos, S., et al. 2015, *MNRAS*, 451, 400  
 Mehta, V., Scarlata, C., Colbert, J. W., et al. 2015, *ApJ*, 811, 141  
 Miyazaki, S., Komiyama, Y., Kawanomoto, S., et al. 2018, *PASJ*, 70, S1  
 Miyazaki, S., Komiyama, Y., Nakaya, H., et al. 2012, in *Proc. SPIE*, Vol. 8446, Ground-based and Airborne Instrumentation for Astronomy IV, 84460Z  
 Moffat, A. F. J. 1969, *A&A*, 3, 455  
 Momose, R., Ouchi, M., Nakajima, K., et al. 2014, *MNRAS*, 442, 110  
 Murayama, T., Taniguchi, Y., Scoville, N. Z., et al. 2007, *ApJS*, 172, 523  
 Ono, Y., Ouchi, M., Harikane, Y., et al. 2018, *PASJ*, 70, S10  
 Ouchi, M., Harikane, Y., Shibuya, T., et al. 2018, *PASJ*, 70, S13  
 Ouchi, M., Ono, Y., Egami, E., et al. 2009, *ApJ*, 696, 1164  
 Ouchi, M., Shimasaku, K., Akiyama, M., et al. 2008, *ApJS*, 176, 301  
 Ouchi, M., Shimasaku, K., Furusawa, H., et al. 2003, *ApJ*, 582, 60  
 Ouchi, M., Shimasaku, K., Furusawa, H., et al. 2010, *ApJ*, 723, 869  
 Page, M. J. & Carrera, F. J. 2000, *MNRAS*, 311, 433  
 Pallottini, A., Ferrara, A., Pacucci, F., et al. 2015, *MNRAS*, 453, 2465  
 Partridge, R. B. & Peebles, P. J. E. 1967, *ApJ*, 147, 868  
 Peacock, J. A. 1983, *MNRAS*, 202, 615

- Petrosian, V. 1992, *Luminosity Function of Flux-Limited Samples*, ed. E. D. Feigelson & G. J. Babu (New York, NY: Springer New York), 173–194
- Piqueras, L., Conseil, S., Shepherd, M., et al. 2017 [1710.03554]
- Press, W. H., Teukolsky, S. A., Vetterling, W. T., & Flannery, B. P. 1992, *Numerical recipes in FORTRAN. The art of scientific computing*
- Pritchett, C. J. 1994, *PASP*, 106, 1052
- Rauch, M., Haehnelt, M., Bunker, A., et al. 2008, *ApJ*, 681, 856
- Sandage, A., Tammann, G. A., & Yahil, A. 1979, *ApJ*, 232, 352
- Santos, S., Sobral, D., & Matthee, J. 2016, *MNRAS*, 463, 1678
- Sawicki, M., Lemaux, B. C., Guhathakurta, P., et al. 2008, *ApJ*, 687, 884
- Schaerer, D., Izotov, Y. I., Verhamme, A., et al. 2016, *A&A*, 591, L8
- Schechter, P. 1976, *Astrophys. J.*, 203, 297
- Schmidt, M. 1968, *ApJ*, 151, 393
- Shibuya, T., Ouchi, M., Harikane, Y., et al. 2018a, *PASJ*, 70, S15
- Shibuya, T., Ouchi, M., Konno, A., et al. 2018b, *PASJ*, 70, S14
- Shibuya, T., Ouchi, M., Nakajima, K., et al. 2014, *ApJ*, 788, 74
- Shimasaku, K., Kashikawa, N., Doi, M., et al. 2006, *PASJ*, 58, 313
- Shioya, Y., Taniguchi, Y., Sasaki, S. S., et al. 2009, *ApJ*, 696, 546
- Sobral, D., Matthee, J., Darvish, B., et al. 2015, *ApJ*, 808, 139
- Sobral, D., Matthee, J., Darvish, B., et al. 2018a, *MNRAS*, 477, 2817
- Sobral, D., Santos, S., Matthee, J., et al. 2018b, *MNRAS*, 476, 4725
- Soto, K. T., Lilly, S. J., Bacon, R., Richard, J., & Conseil, S. 2016a, *MNRAS*, 458, 3210
- Soto, K. T., Lilly, S. J., Bacon, R., Richard, J., & Conseil, S. 2016b, *ZAP: Zurich Atmosphere Purge, Astrophysics Source Code Library*
- Steidel, C. C., Bogosavljević, M., Shapley, A. E., et al. 2011, *ApJ*, 736, 160
- Steinhardt, C. L. & Jermyn, A. S. 2018, *PASP*, 130, 023001
- Taniguchi, Y., Shioya, Y., Ajiki, M., et al. 2003, *Journal of Korean Astronomical Society*, 36, 123
- Tapken, C., Appenzeller, I., Gabasch, A., et al. 2006, *A&A*, 455, 145
- Trujillo, I., Aguerrí, J. A. L., Cepa, J., & Gutiérrez, C. M. 2001, *MNRAS*, 328, 977
- van Breukelen, C., Jarvis, M. J., & Venemans, B. P. 2005, *MNRAS*, 359, 895
- Viiironen, K., López-Sanjuan, C., Hernández-Monteagudo, C., et al. 2018, *A&A*, 614, A129
- Weilbacher, P. M., Streicher, O., Urrutia, T., et al. 2014, in *Astronomical Society of the Pacific Conference Series*, Vol. 485, *Astronomical Data Analysis Software and Systems XXIII*, ed. N. Manset & P. Forshay, 451
- Willmer, C. N. A. 1997, *AJ*, 114, 898
- Wisotzki, L. 1998, *Astronomische Nachrichten*, 319, 257
- Wisotzki, L., Bacon, R., Blaizot, J., et al. 2016, *A&A*, 587, A98
- Wold, I. G. B., Finkelstein, S. L., Barger, A. J., Cowie, L. L., & Rosenwasser, B. 2017, *ApJ*, 848, 108
- Yuan, Z. & Wang, J. 2013, *Ap&SS*, 345, 305